Physics – Uspekhi **67** (10) 961 – 987 (2024) © 2024 Uspekhi Fizicheskikh Nauk, Russian Academy of Sciences

REVIEWS OF TOPICAL PROBLEMS PACS numbers: 82.33.Vx, 82.50.Hp, 95.30.Wi, 97.10.Fy, 98.38.Jw

Evolution of carbon particles from the stage of asymptotic giant branch stars to planetary nebulae: observations, experiments, and theory

M S Murga

DOI: https://doi.org/10.3367/UFNe.2023.12.039614

Contents

1. **Introduction** **961**
2. **Observational data on carbon particles in asymptotic giant branch stars, protoplanetary and planetary nebulae** **963**
   2.1 Main observational features; 2.2 Manifestations of evolutionary processes
3. **Physical conditions in dust formation zones and in evolution of dust** **971**
4. **Formation and evolution of carbon particles: modern theoretical concepts and experiments** **972**
   4.1 From C_2H_2 to dust; 4.2 Effect of oxygen on formation and evolution of polycyclic aromatic hydrocarbons, fullerenes, and dust
5. **Astrochemical experimental studies of interstellar dust analogues** **977**
   5.1 Laboratory synthesis of interstellar dust analogues; 5.2 Optical properties of interstellar dust analogues
6. **Discussion and conclusions** **982**
   References **985**

Abstract. **We review research into the evolution of carbon particles at stages from the envelopes of asymptotic giant branch stars to planetary nebulae. The evolution of carbon particles is discussed from several standpoints: observational data are summarized; the formation mechanisms and clustering of aromatic molecules are considered; conditions for the formation of carbon particles in the envelopes of stars and for their subsequent evolution in protoplanetary and planetary nebulae are described; results of experiments on creating equivalents of interstellar dust and analyzing their characteristics are presented; and, finally, possible evolutionary scenarios for carbon particles are presented. Particular attention is paid to fullerene molecules, which are important for constructing a comprehensive picture of the evolution. Their presence and nonuniform distribution suggest that, depending on the conditions, the formation of carbon particles can follow two paths: via planar or nonplanar aromatic molecules.**

Keywords: carbon particles, dust evolution, polycyclic aromatic hydrocarbons, fullerenes, interstellar medium, envelopes of asymptotic giant branch stars, planetary nebulae

M S Murga [1, 2]
[1] Institute of Astronomy, Russian Academy of Sciences, ul. Pyatnitskaya 48, 119017 Moscow, Russian Federation
[2] Ural Federal University named after the First President of Russia B.N. Yeltsin, ul. Mira 19, 620062 Ekaterinburg, Russian Federation
E-mail: murga@inasan.ru

Received 24 October 2023, revised 29 November 2023
Uspekhi Fizicheskikh Nauk **194** (10) 1017 – 1045 (2024)
Translated by S Alekseev

1. Introduction

Interstellar dust is an important component of the interstellar medium (ISM), participating in many physical and chemical processes. Dust determines the energy balance of the medium via the photoelectric effect and the ionization balance via the recombination of electrons and ions. The dust surface serves as a substrate and, in some cases, a catalyst for chemical reactions; as a result, the chemical composition of the ISM is enriched with molecules whose formation in the gas phase is inefficient. Interstellar dust absorbs, scatters, polarizes, and re-emits stellar light, and is also a building material for the formation of planets. The smallest (nanoscale) components of dust, aromatic hydrocarbons, are representatives of complex organic compounds and biomolecules and are therefore of astrobiological importance. Thus, the study of interstellar dust, especially carbon, in the range from molecules with a single aromatic ring and nanoparticles to large conglomerates of a micron scale is important for the development of many areas of astronomy.

There are two types of interstellar dust: carbon and silicate [1]. According to modern models, dust sizes range from ~ 4 Å to several micrometers [1, 2], with the overwhelming majority of small dust grains ($\lesssim 50$ Å) being carbon. It is currently unknown to what extent dust grains are homogeneous in composition. In some models, silicate and carbon grains exist separately [1, 3], while, in other models, dust grains consist of both silicate and carbon materials. For example, in the THEMIS model [4], carbon grains can be purely carbon, although the structure of the carbon material is heterogeneous, and silicate grains are covered with a carbon mantle, and are therefore heterogeneous in chemical composition. In [5], a model is proposed in which dust grains in size $\lesssim 50$ Å

are homogeneous in composition, while larger grains are conglomerates of smaller carbon and silicate grains. The authors believe that such grains are formed in the ISM due to collisions and coagulation.

Regardless of the model, one of the components of dust is small carbon particles: their presence is indicated by a number of observations. First, the infrared (IR) spectra of emission nebulae contain broad bands at wavelengths from 3 to ~ 20 μm, which correspond to vibrational transitions of polycyclic aromatic hydrocarbon (PAH) molecules, fullerenes, nanosize particles of amorphous carbon, and other carbon particles [6–10]. Second, a feature of the absorption curve at a wavelength of 2175 Å coincides with a jump in the absorption of many types of carbon particles [11–14]. Third, diffuse absorption bands appear along almost any line of sight. Five of these bands have been reliably associated with fullerene molecules C_{60}^{+} [15, 16], and others are also assumed to correspond to carbon-containing molecules [17–19]. In the astronomical literature, it is common to relate nanosize particles and macromolecules to dust particles. In what follows in this paper, we use the term 'particle' for both macromolecules and large dust particles, because this term has become established in the physics and chemistry literature on the study of hydrocarbons. We reserve the term 'dust' as a general name for all particles in the astronomical context.

While the presence of carbon particles in the ISM is by no means in doubt, information about their size, structure, and composition is not definitive. An exception is given by the above-mentioned fullerene molecules, which have been identified both by vibrational transitions in the IR range and by electron transitions in the optical range [9, 15, 20]. Benzonitrile and cyanonaphthalene molecules have also been detected by rotational transitions [21, 22].

It is believed that the main source of carbon particles is provided by asymptotic giant branch (AGB) stars, in which the carbon abundance exceeds the oxygen abundance, i.e., $C/O > 1$ [23].[1] 'Carbon chemistry' occurs in these stars. The mass of carbon stars in the main sequence ranges from ~ 1.5 to $\sim 4M_{\odot}$ [26], but low-metallicity stars with a mass of $\sim 1M_{\odot}$ can be carbon [27, 28]. Also, the relative number of carbon stars increases at low metallicity, which is evident from comparing the number of carbon planetary nebulae (PNe) in our Galaxy and in Magellanic Clouds (MCs) [29].

We note that at $C/O < 1$ all carbon is spent on the formation of the CO molecule and 'oxygen chemistry' takes place. There are also stars where the products of 'carbon and oxygen chemistry' are present simultaneously [30]. The reason for the formation of such stars has not been clearly established; one of the possible reasons is the effective 'dredge-up' of matter from the carbon layers of a star at the final stages of its life, when some amount of the 'oxygen' dust (silicate) has already been formed in the envelope [30]. After this event, 'carbon chemistry' takes over in the envelope, and the reactions and mechanisms of formation of carbon particles are most likely similar to those that operate in carbon stars. In this paper, we therefore focus on 'carbon chemistry,' in which there are no dust particles characteristic of 'oxygen chemistry.'

The AGB stage of a star ends when the burning of helium and hydrogen in the shells surrounding the core stellar ceases. Then, the star transforms into a white dwarf, which is attended by its heating, and the formation of a PN. In the course of the transformation, the star is at the post-AGB stage, and such objects are also called as protoplanetary nebulae (PPNe) in the literature. In this paper, the term PPN is used. The main difference between a PPN and a PN is the value of the effective temperature ($T_{\rm eff}$) of the central source: in a PPN, the central source is relatively cold and is not capable to ionize gas, while the center of a PN contains a hot source with $T_{\rm eff}$ up to 200,000 K, which ionizes the surrounding matter. The threshold value of $T_{\rm eff}$ of the central source, dividing the objects into PNe and PPNe, is between 20,000 and 30,000 K. Above this threshold, lines of ionized hydrogen and oxygen start to arise [31]. In PPNe and PNe, a 'photodissociation' region (PDR) appears in the envelope ejected by the star; this is the region penetrated by ultraviolet (UV) photons with energies up to 13.6 eV. Such photons are capable of dissociating molecules and particles formed at the stage of AGB stars, as well as initiating many other chemical reactions. Because the region of ionized hydrogen is not yet present in the PPN, it can be assumed that the PDR occupies the entire region from the central source to the depth of photon penetration. In PNe, the PDR is located behind the hydrogen ionization front. The region of ionized hydrogen expands over time, and the PDR expands accordingly.

To date, the general picture has been constructed to describe how carbon particles form in the envelopes of AGB stars and then sequentially evolve through the PPN and PN stages and, finally, in the ISM. This picture is based on laboratory studies (in particular, combustion processes) and theoretical models [2, 32, 33]. According to this picture, particles are formed directly in the envelopes of stars and their structure represents a mixture of aromatic rings connected to each other by aliphatic bonds. There is no ordered lattice in such particles; their nature is close to amorphous carbon. Next, the formed particles are exposed to the UV radiation field and shock waves. As a result, their structure changes: they become ordered and aromatic. This rearrangement is accompanied by partial destruction of dust particles, and various hydrocarbon molecules, including PAHs and fullerenes, can enter the gas phase [34]. Subsequently, freely flying PAHs and fullerenes coexist in the diffuse ISM with particles of structured amorphous carbon, which can contain a small amount of aliphatic bonds.

The formation of PAHs, fullerenes, and nanotubes has been studied in physical and chemical laboratories due to their widespread use in industry and modern technologies. In addition, the problem of reducing the emission of PAHs and soot as products of incomplete combustion is actively studied, because they are considered hazardous to human health. To control the number of these hazardous particles, the process and mechanisms of their formation are studied in stages. From the standpoint of astronomy, the process of formation of carbon particles is also interesting, because its detailed understanding would allow explaining observational data on carbon particles in space and describing their characteristics (structure, size, and properties). Despite different goals, astronomers, physicists, and chemists are interested in studying the process of formation, growth, and transformation of carbon particles.

There are some unresolved questions in the theory of evolution of interstellar carbon particles. One of these questions is the sensitivity of carbon particle formation processes to environmental conditions, in particular, to parameters that depend on metallicity. Observations show

[1] Carbon dust can also be formed in the remnants of supernovae [24, 25].

that, at low metallicity, the PAH abundance decreases [35, 36] and the total dust content decreases [37], but the relative abundance of fullerene molecules increases [38, 39]. The correlation between the PAH abundance and metallicity is often explained by the more efficient destruction of PAHs at low metallicity [40, 41]. However, some studies, on the contrary, argue for the low efficiency of the formation of PAHs under such conditions [42].

In this review, we examine in detail the main aspects of the formation and evolution of carbon particles (experiments, conditions for the formation of carbon particles in the envelopes of AGB stars, observations of carbon particles in objects directly related to their formation, and the existing hypotheses and models), analyze and compare available data, and evaluate the existing models. Particular attention is paid to fullerene molecules, which are indicators that dust formation can occur along at least two different evolutionary paths. Various factors that can influence the formation path selected in certain objects are discussed.

2. Observational data on carbon particles in asymptotic giant branch stars and protoplanetary and planetary nebulae

The main observational data on carbon particles are obtained from IR spectra, which are very diverse in PPNe and PNe. These spectra are a combination of the thermal continuum with a peak at a wavelength of about 30–40 μm and a number of emission bands, whose presence, position, and intensity vary from object to object and within a specific object. The spectra can be used to identify the common properties of some objects and trace their evolutionary relations. Below, the main features of the spectra are considered and information on their nature and variability is given. Information obtained from optical and IR color indices is provided in addition.

2.1 Main observational features

2.1.1 Aromatic bands. Emission bands at wavelengths of 3.3, 6.2, 7.7, 8.6, 11.2, 12.7, and 16.4 μm and a number of other less intense bands are observed in a large number of space objects of various types [1, 43–46]. These bands correspond to vibrational transitions in compounds containing aromatic (benzene) rings. It is generally accepted that such compounds are PAHs [47]. Each band is responsible for a certain type of vibration (stretching and bending of C–H, C–C, and C–C–C bonds in or outside the plane of the molecule) or for their combination. The observed IR spectra of cosmic objects do not correspond to the spectrum of any specific PAH particle, but can be described by the total spectrum of an ensemble of several dozen PAHs [48, 49]. The interband ratios of fluxes $I_{\lambda_1}/I_{\lambda_2}$ vary, depending on conditions: they reflect changes in the composition and/or characteristics of the set of PAHs responsible for the appearance of the bands [50–52]. In particular, the flux ratio $I_{3.3}/I_{11.2}$ correlates with the average size of the PAH ensemble, and the $I_{6.2}/I_{11.2}$ ratio correlates with the ionization state of this ensemble [51, 52].

All the main PAH bands can be observed in the spectra of PNe, but the exact position, width, and brightness of the bands relative to each other change as the PNe evolve. The 'classical' IR spectrum observed in many ISM objects, with bands at wavelengths of 3.3, 6.2, 7.7, 8.6, 11.2, 12.7, and 16.4 μm, appears in mature PNe, while the spectra of PPNe and young PNe may look different. In [45], ISM objects were

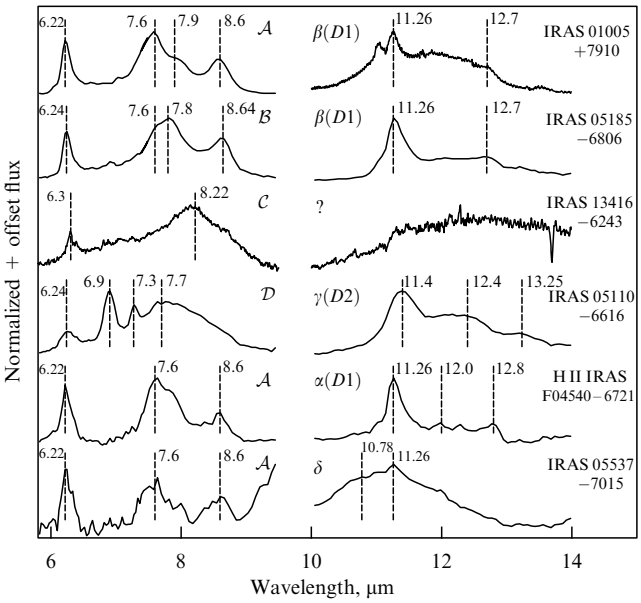

Figure 1. IR spectral classes using the following PPNe as an example: IRAS 01005+7910, IRAS 050185−6806, IRAS 13416−6243, IRAS 05110−6616, IRAS 05537−7015, and the H II region IRAS F04540−6721. Objects are divided into classes $\mathcal{A}$–$\mathcal{D}$ in range of 6–9 μm, and into classes α–δ in range of 11–14 μm. Spectra of objects were taken from archives of ISO (IRAS 13416−6243) and Spitzer (other objects) space telescopes; background subtraction procedure was applied to them.

divided into classes $\mathcal{A}$, $\mathcal{B}$, and $\mathcal{C}$, depending on the position of the bands in the wavelength range of 6–9 μm. Figure 1 (the left part of the spectrum) shows representative IR spectra of these classes. In the class $\mathcal{A}$ spectra (objects IRAS 01005+7910, IRAS F04540−6721, and IRAS 05537−7015), a band at 6.22 μm, a doublet of bands at 7.7 μm with a dominant component at 7.6 μm and a 'shoulder' at 7.8–7.9 μm, and, finally, a band at 8.6 μm are observed. In the class $\mathcal{B}$ spectra (IRAS 05185−6806), the 6.22 μm band is shifted to $\sim$ 6.24 μm, the 7.6 μm component in the 7.7 μm doublet becomes a 'shoulder' for the dominant 7.8 μm component, and the 8.6 μm band is redshifted to 8.7 μm. The $\mathcal{C}$ class spectra (IRAS 13416−6243 in Fig. 1) show a band at 6.3 μm instead of 6.22 μm in class $\mathcal{A}$, and the 7.7 μm doublet is not resolved into bands and is observed as a single broad band peaking at $\approx$ 8.2 μm with a broad red wing down to $\sim$ 9.3 μm, where a small peak at 8.7 μm can be seen.

Class $\mathcal{A}$ can be observed in a wide range of objects: H II regions, reflection nebulae, PNe, PPNe, and Herbig Ae/Be stars; this is arguably the most common type of IR spectra. Class $\mathcal{B}$ is common among PNe, PPNe, and Herbig Ae/Be stars. But class $\mathcal{C}$ was initially found only for PPNe and later extended to include AGB and Herbig Ae/Be stars [53–56].

Objects of class $\mathcal{C}$ have a relatively low effective temperature of the central source (several thousand kelvins), while in objects of classes $\mathcal{A}$ and $\mathcal{B}$, the radiation sources are hotter. It is believed that the appearance of class $\mathcal{C}$ spectra is due to particles that have not yet been exposed to UV radiation and therefore contain aliphatic bonds with lower dissociation energies compared with aromatic bonds [53, 57]. Thus, these particles have a mixed aromatic–aliphatic structure similar to that of hydrogenated amorphous carbon (HAC) with a high relative content of hydrogen. During formation, such particles are dominated by aliphatic bonds and have an

irregular structure, but, under the influence of UV radiation and/or shock waves, they are dehydrogenated and the structure becomes more regular with a large fraction of aromatic rings. As a result of this process, the aliphatic emission bands fade, giving way to aromatic ones [2, 58]. According to [59], small ($\lesssim 200$ Å) dust particles can undergo restructuring in the bulk, while large dust particles change only within the surface layers. Given the evolutionary status and characteristics of objects of classes $\mathcal{A}-\mathcal{C}$, as well as numerous experiments with HAC particles and other analogues, an evolutionary scenario directed from class $\mathcal{C}$ objects through class $\mathcal{B}$ to class $\mathcal{A}$ was proposed [60–62].

PAHs whose total spectrum can describe the spectra of class $\mathcal{A}$ are mainly small, and those for class $\mathcal{B}$ are large [63]. It was suggested in [63] that there is an evolutionary connection between classes $\mathcal{B}$ and $\mathcal{A}$: objects of class $\mathcal{B}$ can transform into objects of class $\mathcal{A}$ under the influence of external factors (radiation and shock waves) and the accompanying destruction of large PAHs. It was not possible to find a suitable set of PAHs for class $\mathcal{C}$ spectra.

In [64], another class of spectra was introduced, $\mathcal{D}$ (object IRAS 05110−6616 in Fig. 1). In the spectra of this class, a wider band at 6.24 μm and one wide band centered at approximately 7.7 μm are observed. Additionally, in contrast to classes $\mathcal{A}$, $\mathcal{B}$, and $\mathcal{C}$, there is a band at 6.9 μm and sometimes a band at 7.3 μm, which are associated with vibrations of aliphatic bonds (see below). The band at 6.9 μm is also observed in the class $\mathcal{B}$ spectra, but is shifted closer to 6.8 μm there. It was shown in [65] that the class $\mathcal{D}$ spectrum can be obtained by a linear combination of the spectra of classes $\mathcal{B}$ and $\mathcal{C}$, but only in the wavelength range of 7–9 μm, while the spectrum in the range of 11–14 μm cannot be reproduced in this way. For the spectra of class $\mathcal{D}$, as well as of class $\mathcal{C}$, it was not possible to select a set of PAHs.

As regards the spectra in the wavelength range of 11–14 μm, it has been suggested to divide them into other classes. In [64], a division into classes α, β, γ, and δ was proposed. The spectra of objects of these classes are presented in Fig. 1 (right side). In the spectrum of class α (H II region IRAS F04540−6721), bands at 11.3, 12.0, and 12.8 μm are clearly visible, and the local continuum under these bands is small. In β class spectra (IRAS 01005+7910 and IRAS 05185−6806), the band at 11.3 μm is broader, the bands at 12.0 and 12.7 μm are either unclear or indistinguishable, and the local continuum is more noticeable. In γ class spectra (IRAS 05110−6616), the local continuum is even larger, and instead of the band at 12.7 μm, bands at $\approx$ 12.3–12.4 and 13.3 μm are visible. And finally, the δ class spectra (IRAS 05537−7015) have a large local continuum ranging from 10 to 12–13 μm with a band at 11.3 μm and sometimes a band at $\approx$ 10.5–11 μm.

In [66], the spectra of objects in the range of 11–14 μm were divided into classes D1, D2, and 'big 11'. The spectra of classes D1 and D2 are PAH-like: the local continuum extends from $\sim$ 10.5 to $\sim$ 13–14 μm with a center near 12 μm, on which the emission bands are located (objects IRAS 01005+7910, IRAS 05185−6806, IRAS 05110−6616, and IRAS F04540−6721 in Fig. 1). A comparison can be made between classes D1–D2 and $\alpha-\delta$ from [64]: class D1 includes classes α and β, and class D2 is the γ class. Objects with spectra corresponding to the δ class are not PAH-like: the local continuum is located at wavelengths from $\sim$ 10 to $\sim$ 12–13 μm with the center at 11.3 μm. Emission bands can be superimposed on it, but their intensity is significantly lower than the intensity of the continuum itself (IRAS 05537−7015 in Fig. 1). Sloan et al. [66] assign such spectra to the 'big 11' group, which is discussed below.

It is impossible to directly compare the $\mathcal{A}-\mathcal{D}$ and $\alpha-\delta$ classes, because two objects of the same class in the 6–9 μm range can belong to different classes in the 11–14 μm range, as can be seen from Fig. 1. For example, the object IRAS 01005+7910 belongs to the $\mathcal{A}$ and β classes, and the object IRAS 05537−7015 also belongs to the $\mathcal{A}$ class in the 6–9 μm range, but to the δ class in the 11–14 μm range.

The δ class spectra are observed predominantly near PPNe, and β and γ class objects also tend to have a relatively cool central source, while α class objects are heated by a hot source. It is impossible to say definitively whether the particles responsible for the emergence of features in the spectra of different objects have anything in common. Perhaps, as in the case of the 'evolutionary' sequence of spectra from class $\mathcal{C}$ to class $\mathcal{A}$, it is possible to trace the change in hydrocarbon material in the transition from the δ to α class. In contrast to the well-studied wavelength ranges of 3–4 and 6–9 μm, there are significantly fewer theoretical and experimental data for the range of 11–14 μm, which does not allow drawing more definitive conclusions about the source of the bands in this range.

2.1.2 Aliphatic bands. The bands at wavelengths of 3.4, 6.9, and 7.3 μm arise as a result of transitions caused by vibrations of aliphatic bonds C–H in hydrocarbon particles [2, 8, 65]. It has not yet been unambiguously established which specific compounds are responsible for the appearance of these bands in the ISM. Many variants have been proposed in the literature: super-hydrogenated PAHs [67, 68], PAHs with methyl and methylene functional groups [69, 70], HAC particles [2, 71, 72], mixed aliphatic–aromatic organic particles (MAON) [10], and coal [73].

The aliphatic band at 6.9 μm is observed in objects of class $\mathcal{D}$. Can objects of this class be included in the evolutionary scenario $\mathcal{C} \to \mathcal{B} \to \mathcal{A}$ presented above? On the one hand, the presence of a band at 6.9 μm in the spectra of this class indicates the largest number of aliphatic bonds compared to other classes, i.e., class $\mathcal{D}$ is apparently the initial stage of particle evolution, preceding objects of class $\mathcal{C}$. On the other hand, the $\mathcal{D}$ class spectra can be obtained by a linear combination of the $\mathcal{B}$ and $\mathcal{C}$ class spectra, in which case the $\mathcal{D}$ class is an intermediate link between $\mathcal{B}$ and $\mathcal{C}$. However, the 6.9 μm band is not observed in the $\mathcal{C}$ class spectra, whereas it should be present in 'younger' material. Jensen et al. [65] suggested that the $\mathcal{C}$ and $\mathcal{D}$ class objects are not evolutionarily related and represent different branches in the grain formation process. Recall that, unlike the $\mathcal{A}$ and $\mathcal{B}$ classes, no set of PAHs could be found for the $\mathcal{C}$ and $\mathcal{D}$ class spectra, and hence the particles of these classes are different in nature from isolated PAHs in the gas phase [63]. It is likely that particles of classes $\mathcal{C}$ and $\mathcal{D}$ represent different types of 'astrosoot' with different structures and different hydrocarbon domains, and their arrangement relative to each other differs, resulting in different optical properties.

An important indicator of the 'aliphaticity' degree of the particles is the band at 3.4 μm, which should be brighter than those at 6.9 and 7.3 μm [61]. Spitzer[2] telescope spectrographs did not cover this wavelength range, while most of the conclusions were made based on the data from this tele-

[2] https://www.spitzer.caltech.edu/.

scope. Information about this range was obtained from other telescopes, such as the ISO[3] and Akari[4] space telescopes, as well as from ground-based telescopes, for example, from the UKIRT[5] telescope. The band at 3.4 μm was found both in absorption and in emission. In [7], observations of the PPN CRL 618 were carried out, and absorption in this band was recorded in the spectrum, which implies the presence of carriers of this band in the matter ejected by the star at the AGB stage. The same spectra show a band at 3.3 μm, but in emission, which indicates different spatial positions of the carriers of the bands at 3.3 and 3.4 μm.

Observations of the emission band at 3.4 μm are presented in [74]. It is shown that the ratio of the intensity of the aliphatic band at 3.4 μm, $I_{3.4}$, to the intensity of the aromatic band at 3.3 μm, $I_{3.3}$, increases with increasing $T_{\rm eff}$ to $\approx$ 50,000 K, and then stays at approximately the same level. At the same time, $I_{3.3}$ relative to the total IR intensity decreases with increasing temperature to $T_{\rm eff} \approx 50{,}000$ K, and then increases. The authors suggest that, at the first stage up to $T_{\rm eff} \approx 50{,}000$ K, the observations reflect the destruction of PAHs responsible for the emission at 3.3 μm, whereas, as the H II region expands, the radiation from the star reaches more distant regions and excites a larger number of PAHs, but the destruction no longer occurs at the same rate due to the longer distance from the star and a larger volume of dust with the same number of ionizing photons. Based on the fact that $I_{3.4}/I_{3.3}$ increases, the authors conclude that PAHs in regions distant from the star are more saturated with hydrogen and attach groups with aliphatic bonds. It remains unclear why the increase in $I_{3.4}/I_{3.3}$ terminates and why the destruction of aliphatic bonds is not reflected in the behavior of the band at 3.4 μm. The picture is complicated by observations presented in [75], which show that the $I_{3.4}/I_{3.3}$ ratio decreases with distance from the star: as the PDR expands and $T_{\rm eff}$ increases, a decrease in $I_{3.4}/I_{3.3}$ should be observed, and not an increase, as in [74]. To arrive at more substantiated and consistent conclusions, simultaneous observations of all the main aromatic and aliphatic bands are required, together with theoretical calculations of how the band ratios should change as the PDR expands and PAHs and other carbon particles are destroyed.

2.1.3 Fullerene bands. Fullerene molecules (C_{60}, C_{60}^{+}, and C_{70}) have several vibrational transitions, the principal ones being at the wavelengths of 7.0, 8.5, 17.4, and 18.9 μm [9]. These transitions (except the band at 18.9 μm) often overlap with the PAH bands, which imposes a limitation on the assessment of the intensities of the bands of both PAHs and fullerenes.

To date, fullerenes have been detected in 24 PNe [76], which is only about a few percent of all carbon PNe. The morphology of PNe containing fullerenes (C_{60}-PNe hereafter) can be different. Their nonuniform metallicity distribution is noticeable: their relative abundance increases with decreasing metallicity, which was established by comparing the abundance of C_{60}-PNe in the Galaxy and in the Large and Small Magellanic Clouds (LMC and SMC) [29]. Galactic C_{60}-PNe also have reduced metallicity [39]. The elemental composition of C_{60}-PNe corresponds to the initial mass of a star in the range from ≈ 1.5–$2.5 M_{\odot}$, while the reduced argon abundance in them suggests that such stars belong to the old population [39]. A comparison of PNe with and without C_{60} showed that their elemental compositions are similar, with the possible exception of nitrogen [39, 76]. In [76], it was shown that, in C_{60}-PNe, iron is largely found in dust, and not in gas. It is noteworthy that the two PNe with the strongest fullerene bands, Tc 1 and Sast2-3, have lower carbon abundances in their gas than another C_{60}-PN, IC 418, which has weak fullerene bands. The C/O ratio is lower in Tc 1 than in IC 418. Otsuka et al. [77] note that the carbon abundances in C_{60}-PNe are lower than in C_{60}-free PNe for a sample of PNe in the SMC, but the sample is very limited. On the other hand, the carbon abundances in the gas of Galactic C_{60}-PNe and C_{60}-free PNe are comparable, whence Otsuka et al. [76] conclude that the carbon abundance, relative to oxygen in particular, does not affect the fullerene abundances and that the formation of fullerenes is instead influenced by the properties of the central star.

In addition to fullerenes being more common at lower metallicity, they are observed only in PNe with a relatively low $T_{\rm eff}$ of the central star ($\approx$ 30,000–50,000 K) and in PPNe, i.e., in objects that are in a low-ionization state [38, 39, 76]. Indeed, fullerenes are observed only in relatively young PNe and in PPNe. The reason why fullerenes are not observed in mature PN is unclear. One explanation may be that the fullerene bands become invisible against the background of dust and PAH emission when irradiated by a powerful UV source with $T_{\rm eff} \gtrsim 50{,}000$ K.

Cami et al. [78] studied the spatial distribution of dust, ionized gas, and fullerene emission in the PN Tc 1. According to this study, these three components are located at different distances from the star. The closest to the star is coarse dust and probably PAHs, next is ionized hydrogen H II, and fullerenes are already at the boundary between the H II region and the PDR. Thus, fullerenes are visible in the areas where the radiation field is lower than where dust and PAHs are observed.

In [39], the flux ratio $I_{3.3}/I_{11.2}$ between the 3.3 and 11.2 μm bands in C_{60}-PNe was compared with that in C_{60}-free PNe PAHs and was shown to be lower in C_{60}-PNe. This may indicate that the average size of PAHs in them is smaller than C_{60}-free PNe PAHs. The spectra of C_{60}-PNe correspond to the spectra of class $\mathcal{A}$.

The discovery of fullerenes and the nonuniformity of their distribution among PNe raise a number of questions about the evolution of carbon particles. In particular, what exactly are the fundamental differences among their formation scenarios at different metallicities? Namely fullerenes can be a kind of litmus test for determining the scenario according to which carbon particles were formed in a particular object and under particular conditions.

2.1.4 Local continuums at wavelengths of $\sim$ 8, 12, and 17 μm. The emission bands described above 'sit' on some bumps or, in other words, on small local continuums (often called plateaus in the literature). These plateaus are wide (approximately several μm), and their centers fall at wavelengths of $\sim$ 8, 12, and 17 μm. Figure 2 shows the spectrum of the PPN IRAS 1005 + 7910, where the global continuum from the thermal emission of large dust grains is highlighted in blue and three local continuums, extending from approximately 6 to 9 μm, from 10 to 14 μm, and from 15 to 18 μm, are highlighted in red.

Plateaus are observed not only in PPNe and PNe but also in other ISM objects, although their size and shape may vary

[3] https://www.cosmos.esa.int/web/iso.
[4] https://www.isas.jaxa.jp/en/missions/spacecraft/past/akari.html.
[5] https://about.ifa.hawaii.edu/ukirt/about-us/.

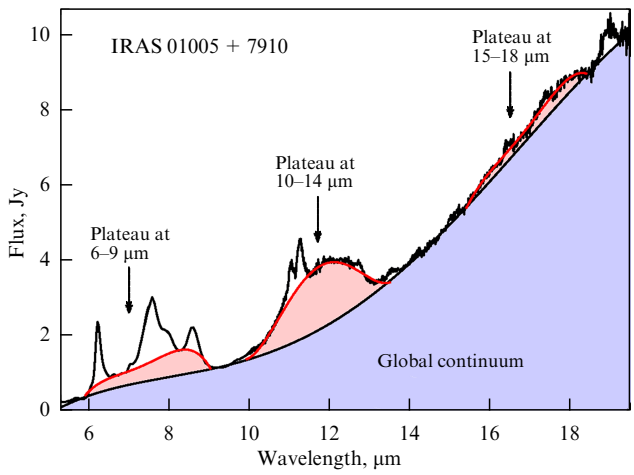

Figure 2. IR spectrum of PPN IRAS 01005+7910. Global continuum is shown in blue, and local continuums at wavelengths of 6–9, 10–14, and 15–18 μm are shown in red. (Spectrum is taken from the Spitzer space telescope archive.)

from object to object. Unlike emission bands, which can at least be attributed to a certain type of oscillation, if not to a specific molecule, plateaus can probably be explained by a combination of different oscillations. The particles in which the oscillations occur can be pronouncedly nonplanar: three-dimensional PAH clusters, HAC particles, and MAONs [57, 79–81]. Joblin et al. [57] note that these plateaus correlate with the presence of an aliphatic band at 6.9 μm, which confirms a connection with some aliphatic structures. As PNe evolve, the aliphatic bands gradually disappear, and the plateau size also decreases [57, 75]. In contrast, aromatic bands become dominant in the mid-IR spectra with the PNe age.

The plateaus at 8 and 12 μm are present in the spectra of C_{60}-PNe. For example, in the spectrum of the PPN IRAS 01005+7910 (see Fig. 2), a broad band is seen at 18.9 μm, similar to those corresponding to the C_{60} band in C_{60}-PNe, indicating the presence of fullerenes. The simultaneous presence of plateaus and bands of fullerenes gave reasons to assume that fullerenes are the result of photodissociation of HAC particles [38, 82]. However, plateaus are found among PNe much more often than fullerene bands, and therefore, if a connection between HACs and fullerenes exists, it is not direct and there must be additional factors influencing the process of fullerene formation from HACs.

2.1.5 Feature at a wavelength of 11.3 μm. A feature at a wavelength of 11.3 μm is observed in the spectra of AGB carbon stars, PPNe, and PNe [66, 83]. This band is strong and narrow at the early stages of the evolution of an AGB star, but, as it evolves and the opacity of the stellar envelope increases, the band becomes wider and flatter [84]. The band brightness is lower for low-metallicity stars [28]. For Galactic objects, this feature disappears at the PPN stage and rarely appears at the PN stage. However, it is widespread and quite pronounced in MC PNe [64, 66, 83]. It can coexist with broad aromatic bands, but its brightness decreases with increasing radiation field hardness [83]. The brightness of the feature at 11.3 μm also anticorrelates with the brightness of the fullerene bands [66].

In most studies, this feature is associated with silicon carbide (SiC) particles [84, 85]. This explains the decrease in the brightness of this feature in low-metallicity stars because of their lower silicon abundance. For Galactic stars, the brightness of the SiC feature correlates with the amount of hot dust [86]. It is assumed that, in the envelopes of Galactic stars, SiC particles are formed before carbon particles, because SiC has a higher condensation temperature. When the envelope cools after the formation of SiC particles, condensation of carbon particles begins, which can settle on the SiC particles and form a carbon mantle [87, 88]. By the end of the AGB star and PPN stages, the SiC cores are already covered with such a mantle, which is why they do not manifest themselves in the emission spectra. The fading of the feature at 11.3 μm is also associated with self-absorption [89]. In PNe, under powerful UV radiation, part of the carbon mantle can be desorbed, as a result of which the feature at 11.3 μm can reappear.

A somewhat different pattern applies to AGB stars, PPNe, and PNe in the MCs. The brightness of the 11.3 μm feature of AGB stars in the MCs is not only lower than in the Galaxy but also appears in stars that are 'redder' in IR color indices and at a lower dust temperature than those in the Galaxy [86, 88]. In MC PPNe and PNe, this feature is wide and pronounced [64, 66, 83]; it is also called the 'big 11.' It is believed to arise in MC PPNe and PNe as a result of the combination of PAH and SiC emission [64, 66]. The presence of a strong SiC feature in MC PPNe and PNe contradicts the above-described particle condensation sequence SiC $\rightarrow$ C and is also inconsistent with the presumed low intensity due to the low silicon abundance. It was assumed in [66, 88] that, at low metallicity, the condensation temperature of SiC is lower than that of carbon particles due to the low concentration, and therefore carbon particles are formed first, after which a SiC mantle settles on the carbon core, possibly mixed with carbon particles, which also continue to be formed. The effect of metallicity on the condensation temperature of SiC and graphite was studied in [90], with the conclusion that both condensation temperatures are indeed lower at lower metallicity, but it was also established numerically that SiC particles are still the first to be formed, after which both carbon and SiC particles start settling down on these seeds simultaneously.

The authors of [64, 82, 91] demonstrate that the shape of the 'big 11' feature must be analyzed in each PN individually, because its shape can be indicative of its nature. We consider examples of IR spectra of different objects in the vicinity of the 11.3 μm feature shown in Fig. 3a. For each object, the profile of the observed feature was fitted by a parabolic function in order to demonstrate the overall shape without noise and superimposed lines. Only the resultant parabolic functions are shown in Fig. 3b.

The classical shape of the feature at 11.3 μm in the spectrum of a star is shown using the example of the star MSX SMC 159 (SMC). In the MC PPNe, this feature looks similar, which is shown by the example of the PPN SMP LMC 058 (LMC) from the sample in [66]. If we ignore the band at $\approx$ 10.5 μm corresponding to the [S IV] line, we can see that the 11.3 μm feature in this object is very close to that observed in AGB stars: the parabolic functions fitted to SMP LMC 058 and MSX SMC 159 are virtually identical. The feature in SMP LMC 058 has a small prominent peak at $\sim$ 11.3 μm, narrower than the main band. This wavelength is that of one of the vibrational transitions of PAHs. Sloan et al. [66] concluded that the contribution of SiC to this feature is about 90%, with the remainder being due to PAHs, as evidenced by the band at 11.3 μm.

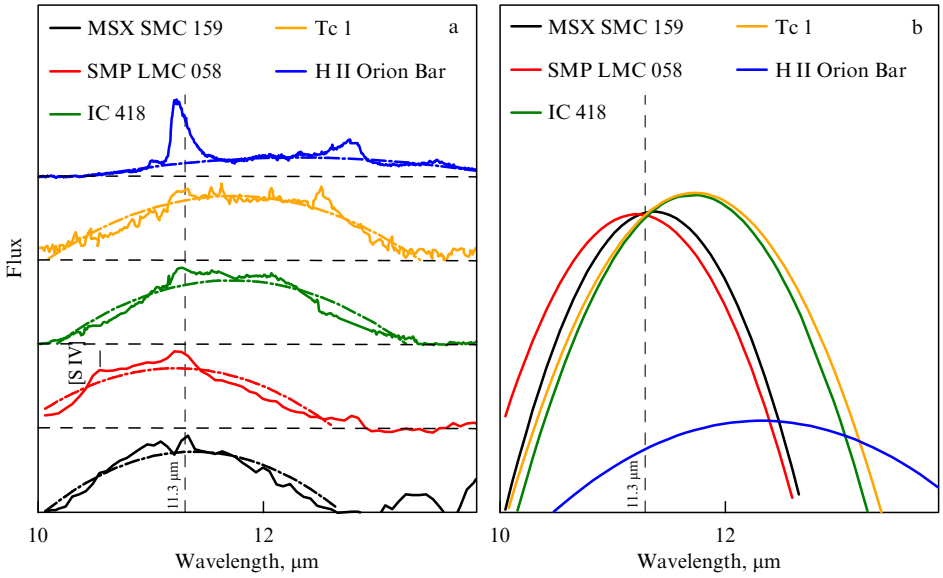

Figure 3. (a) IR spectra in the vicinity of 11.3 μm feature for objects with continuum background subtracted (from bottom to top): AGB star MSX SMC 158, PN SMP LMC 058 (LMC), PNe IC 418 and Tc 1 (both in the Galaxy), and PDR around H II region in Orion Bar. Spectra of MSX SMC 158, SMP LMC 058, and IC 418 are taken from Spitzer telescope archive, Orion Bar spectrum is taken from ISO telescope archive, and Tc 1 spectrum is adapted from [82]. (b) Parabolic functions obtained by fitting to observational data in Fig. a.

The spectra of Galactic PNe are represented by the examples of objects IC 418 and Tc 1. They exhibit a broad band in the wavelength range of 10–14 μm, but it is clear that the feature is shifted toward longer wavelengths with a small peak at $\sim$ 11.3 μm. As a result of a detailed analysis of this band in the spectra of Galactic PNe, including IC 418, Otsuka et al. [39] suggested that the spectral feature in this range is explained by thermal emission from dust and is related to PAHs rather than SiC: the SiC material is densely covered by the mantle and does not show up. Bernard-Salas et al. [82] concluded that, in the case of Tc 1 and a number of other PNe, this feature is not related to SiC either, but is rather caused by the emission of HAC particles, whose spectra contain broad features at these wavelengths [2, 92]. A similar standpoint is shared by the authors of [10, 93], where MAONs, which are generally similar in structure to HAC particles, are proposed to explain the 11.3-μm band. In turn, Ohsawa et al. [94] demonstrated the spectrum of the Galactic PN G095.2+00.7, which contains a prominent 'big 11' band but lacks a band at 3.4 μm, which would indicate the presence of any hydrogenated particles. But, first, their spectra at 2.5–5 μm and at 5–14 μm were obtained on different devices with significantly different characteristics, including spatial resolution, and hence there is no absolute certainty that we are seeing the spectra of the same object (in terms of its spatial size). Second, dehydrogenated HAC can create a plateau at 10–14 μm but still not exhibit a band at 3.4 μm [2]. Thus, in Galactic PNe, the feature at 11.3 μm is similar to the local continuum at $\sim$ 12 μm discussed above, and the particles responsible for its occurrence are therefore similar.

For comparison, Fig. 3 shows the spectrum of the Orion Bar PDR as an example of an object with an IR spectrum typical for emission nebulae. The spectrum contains a broad feature in the wavelength range of 10–14 μm, but it is much wider and flatter than those in the spectra of AGB stars, PPNe, and PNe. Spectra with such a local continuum can be explained by the total spectrum of a set of PAHs [49], the emission of PAH clusters, the above-mentioned HAC particles, or other carbon particles [57, 95].

Today, in sum, the feature at 11.3 μm in AGB stars is most likely associated with SiC particles, but in the spectra of PNe (especially Galactic ones), this feature can be associated with carbon particles rather than SiC or with particles that include both carbon material and SiC. For an accurate detailed analysis and assessment of the contributions from each of the materials, it is necessary to know the exact optical constants of the materials of these particles. The optical constants for the crystalline forms of SiC, α-SiC, and β-SiC [96, 97] and the amorphous form of SiC [98] are available in the literature. The model spectrum of β-SiC particles (taking their shape and size distribution into account) is closest to that observed in AGB stars, and, in addition, most of the SiC material in meteorites is in this form [84, 97]. The optical constants for the HAC particles and PAH clusters, which are associated with the continuum centered at 12 μm, are also presented in the literature [59, 81], but the model spectra of the HAC particles do not describe this wavelength range accurately (see Fig. 7 in [82]). Moreover, as noted above, as an AGB star evolves, the SiC particles are covered by a carbon mantle at high metallicity, whereas, at low metallicity, SiC and carbon condense simultaneously. The parameters and properties of such mixed particles (size, shape, porosity, and optical constants) are not known, and therefore an accurate analysis of observations and the assessment of the contribution of each component are currently difficult. A correct analysis of the spectra might lead to alternative conclusions about the nature of the 11.3 μm feature in PPNe and PNe and its relation to other features of the IR spectra.

2.1.6 Feature at 21 μm. The feature at 21 μm is observed quite rarely and only at the PPN stage [91]. According to [99], it was detected in 31 sources in the Galaxy and the MCs, and it is weaker in MC objects, indicating a dependence on metallicity. It is noteworthy that its position hardly varies at all from

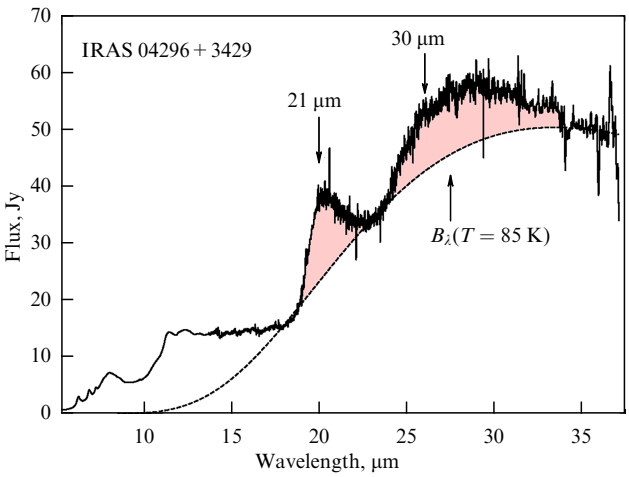

Figure 4. IR spectrum of PPN IRAS 04296+3429. The Planck function corresponding to a temperature of 85 K is drawn with a dashed line. Features at 21 and 30 μm are highlighted in pink. (The spectrum is taken from Spitzer telescope archive.)

object to object. An example of a spectrum with the 21 μm feature is shown in Fig. 4.

It was found in [66] that all objects exhibiting the 21 μm feature belong to the $\mathcal{D}$ class in the range of 7–9 μm, and most of them belong to the D2 class in the range of 11–14 μm. Their spectra clearly show plateaus at 8 and 12 μm, and the plateaus dominate relative to the emission bands in Galactic objects, but are lower in brightness than the bands in MC PPNe. The spectra of objects with a feature at 21 μm contain aliphatic bands at 6.9 and 7.3 μm and bands at 15.8 and 17.1 μm, which presumably arise as a result of bond vibrations in alkynes (hydrocarbons with a triple bond). We note that all class $\mathcal{D}$ objects are relatively cold: their central sources have spectral classes F or G. Probably, carriers of the feature at 21 μm can exist or reveal themselves only under such irradiation conditions [64].

Besides plateaus at 8 and 12 μm, spectra with the 21 μm feature also contain a feature at 30 μm (see below) [66], but not all objects with the 30 μm feature contain the 21 μm feature.

There is currently no established opinion on the carrier of the 21 μm feature. Volk et al. [99] compiled a list of options proposed in the literature, which includes nanodiamonds [100], titanium carbide particles [101], iron oxides [102], and many others. However, based on the association of the spectra with the 21 μm feature with particles possessing aliphatic bonds, and given the evolutionary status of objects with this feature, the most logical hypothesis is apparently that some complex hydrocarbons, including aromatic and aliphatic bonds with a partially amorphous and partially aromatic structure, are responsible for its occurrence [99]. The appearance of a feature at 21 μm at the intermediate and short stage of stellar evolution suggests that it reflects some intermediate state of dust grains during the transition from the amorphous to the aromatic state [66]. In [108], a small feature at 21 μm was detected in the spectrum of HAC particles, but additional measurements are required to establish an unambiguous connection with HAC. Theoretical calculations of the spectra of bulk particles with a complex aromatic–aliphatic structure are also necessary, which is a complex and somewhat ambiguous problem.

2.1.7 Feature at a wavelength of 30 μm. A very broad feature is observed at a wavelength of 30 μm, whose nature has not been unambiguously established. It is shown in Fig. 4 in the same spectrum as the feature at 21 μm. To make the 30 μm feature more clearly visible, the continuum from the thermal emission of dust fitted by the Planck function with a dust temperature of 85 K is drawn in the figure, with the 30 μm feature rising above it. This feature can appear both at the stage of AGB stars and in PPNe and PNe. It is more common than the 21 μm feature, but is not present in all objects. Gladkowski et al. [103] noted that the shape of the feature changes when moving from AGB stars and PPNe to PNe. The brightness of the 30 μm feature is higher for AGB stars in the Galaxy and lower for MC stars, indicating a dependence on metallicity [86], but this tendency disappears if we consider PPNe and PNe [103]. In the stars of the Galaxy, the feature appears at different stages of stellar evolution, including when the dust temperature has its maximum values (> 900 K), whereas in the LMC and SMC, it appears only when the dust temperature decreases, respectively, to 900 and 700 K [103]. The brightness increases as the dust cools to ≈ 400 K, i.e., the redder the object, the brighter the feature at 30 μm. As soon as the dust temperature drops to ≈ 400 K and the maximum mass loss occurs, the brightness of this feature decreases significantly or disappears completely, possibly due to self-absorption. But at the PPN stage, the feature reappears, and its brightness reaches high values.

The position of the peak of the feature at 30 μm varies from object to object within the range from ≈ 26 to ≈ 33 μm [103]. The average value of the peak wavelength is about 29 μm for AGB stars and PPNe and about 30–31 μm for PNe. Hony et al. [104] suggested that such a shift is associated with a change in the temperature or shape of the particles. In turn, Gladkowski et al. [103] believe that the shift is a consequence of a change in the structure and properties of the material itself due to the action of the UV radiation field, but not a change in temperature. The position of the peak has a longer wavelength in the MC PNe, and hence these changes should be more effective in the MCs.

It is believed that magnesium sulfide (MgS), possibly together with iron and calcium sulfides, is responsible for the formation of this feature [87, 105]. Zhukovska and Gail [106] showed that the condensation and formation of individual MgS particles is inefficient and that these particles are more likely to condense on the surface of existing dust grains, namely, SiC. This scenario can be supported by the fact that the 30 μm feature is anticorrelated with the 11.3 μm feature (SiC) described above: for AGB stars, its brightness increases as the brightness of the SiC feature decreases [88, 106].

Although the MgS hypothesis is widely accepted among researchers, other proposals have also been put forward. For example, Otsuka et al. [39] showed that the continuum emission and the strength of the 30 μm feature are correlated and must therefore share the same carrier, namely, carbon particles. In [39, 107], it is shown that the feature can be described by graphite dust grains, and in [108], particles of amorphous carbon are proposed. The main advantage of the hypothesis about the carbon carrier is that it is consistent with the absence of a correlation between the brightness of the feature and the metallicity in PNe, but there is still no unambiguous data on the resonance of carbon materials at the corresponding wavelengths and its variation with temperature.

2.1.8 Continuum. It is generally accepted that particles of amorphous carbon or HAC are responsible for the emergence of the IR continuum in AGB stars, PPNe, and PNe [87, 109–114], because amorphous carbon satisfies the observed dependence of the emissivity on the wavelength, $k \propto \lambda^{-1}$, at long wavelengths. Graphite particles have also been proposed to describe the continuum, but such a dependence for them is different: $k \propto \lambda^{-2}$ according to [115]. Men'shchikov et al. [87] note that dust grains in PNe should be heterogeneous in composition, be porous and loose, and also have a non-spherical shape. From the standpoint of these authors, it is impossible to explain the observations only by graphite material, whereas conglomerates containing amorphous carbon, silicon carbide, and magnesium sulfide can explain the IR spectra, including the continuum and the features at 11.3 and 30 μm.

2.1.9 Fluxes in photometric bands and color indices. Photometric color indices are widely used to study all stages of the evolution of AGB stars — from late combustion stages to PNe. Both optical color indices (e.g., in the UBV system) and IR color indices are used, but the latter are more informative, especially for late stages of AGB stars, because such objects are too faint in the optical range due to the thick dust shell surrounding them. Using color–luminosity diagrams compiled from the 2MASS catalog in the JHK photometric system, we can, first, separate oxygen and carbon stars and, second, establish at what stage of its evolution the star is as regards dust production, because, with an increase in the mass loss of the star and dust production, the luminosity (for example, in the K filter) decreases, while the color indices (for example, J–K) increase. However, the assignment of a particular characteristic to a star based on the JHK system is often ambiguous. With the advent of the Spitzer telescope, a new color system in the IR range was developed specifically for the analysis of AGB stars and PPNe: the 'Manchester' system [116]. The system uses four bands with central wavelengths at 6.4, 9.3, 16.5, and 21.5 μm. The fluxes in these bands are measured from the spectra. The 'Manchester' color indices [6.4]–[9.3] and [16.5]–[21.5] are used to characterize objects and classify them. The [6.4]–[9.3] color index for stars indicates whether the stellar photosphere or dust dominates in the spectrum, or, in other words, serves as a measure of the optical thickness of the envelope and also a measure of the rate of dust production [117]. The [16.5]–[21.5] color index characterizes the dust temperature. An analysis of the 'Manchester' color indices of a large sample of AGB stars revealed that the dust production rates are comparable for low- and high-metallicity stars, with the exception of individual stars with extremely low metallicity ($[\mathrm{Fe/H}] < -1.0$), for which the dust production rate is lower [28, 117]. This contradicts the results of theoretical modeling, according to which dust is produced less efficiently at low metallicity than at high values [28].

Measurements in the standard photometric bands of the Spitzer telescope at 3.6, 4.5, 5.8, 8.0, and 24 μm are also used for the analysis. Based on the color [8]–[24] and [4.5]–[8] indices, it is possible to clearly separate AGB stars and PPNe, because the latter have already begun to remove the envelope and cool, which leads to an increase in these color indices. At the same time, near-IR color indices (e.g., J–K) decrease as the central sources become less obscured by dust.

Sloan et al. [66] found that PNe containing C_{60} but not PAHs have a narrow range of IR color indices ranging from near-IR (K_s–[3.6]) to mid-IR ([8]–[24]), while C_{60}-PNe and PAHs have a wider range. This may indicate that the conditions under which fullerenes are observed are different from those under which PAHs are observed. It was also shown in [66] that C_{60}-PNe are 'bluer' in the optical colors ([U–B] and [B–V]) than all other PNe and PPNe, although the IR colors indicate a significant dust amount. The authors of [66] concluded that dust and fullerenes are spatially separated in such objects, i.e., there is little dust in the line of sight, where fullerenes are observed. They hypothesized that the discrepancy between the optical and IR color indices may be due to the presence of a disk in the PNe. A disk can appear in a PNe when a binary star is located at the center [118]. If the disk is visible to the observer face-on, then there is less absorption along the line of sight, and the optical color indices are lower than when the disk is seen edge-on. Also observed in the face-on position are fullerenes that for some reason are spatially located in the inner parts of this disk, while dust and PAHs are located in the outer parts. However, the authors note that the low spatial resolution of IR observations does not allow separating different parts of the disk.

Otsuka et al. [77] have shown that the C_{60}-PN Lin 49 and a number of other C_{60}-PNe in fact exhibit an excess of luminosity in the central region in the near-IR bands, indicating the presence of a dense substructure around the central star, the disk. In contrast to [66], where the possibility of observing fullerenes is associated with the geometric position of the disk, the authors of [77] believe that the conditions in the disk (high density and temperature) are favorable for the formation of fullerenes.

Objects with the 21 μm feature occupy a position opposite to fullerenes on the [U–B]–[B–V] diagram and are 'redder' objects. The other PNe and PPNe are located between these two types. The temperature of objects with the 21 μm feature is very low, about 7000 K on average, and they are more obscured by dust than other types of PPNe and PNe, indicating their early evolutionary stage and hence the earliest state of dust in them [66].

The bolometric values of C_{60}-PNe overlap with those for objects where the 'big 11' feature and a set of other features, including PAHs, are observed, while objects with features similar to PAHs (but not classical PAH features) and 21 μm (except class D2 PPNe) are brighter [66]. The division into groups by brightness probably indicates a common nature within each group.

2.2 Manifestations of evolutionary processes

In this section, we give additional information on the behavior of IR features and their relations to each other, and also present a summary of the available observations in the form of a schematic illustration that allows drawing conclusions about the evolution of dust from AGB stars to PPNe (Fig. 5). Of greatest interest is probably the short evolutionary stage of PPNe and young PNe, where a great diversity of IR spectra is observed. In Fig. 5, we outline the possible relations and evolutionary transitions between IR features, although these relations are not always unambiguous, and in some cases are therefore shown with dashed lines.

At the AGB star stage, the amount of dust estimated from color indices is independent of metallicity [117, 119]. On the other hand, the acetylene (C_2H_2) bands (the very first precursor of PAHs and dust) at wavelengths of ≈ 7.5 and 13.7 μm are more intense in MC objects than in Galactic

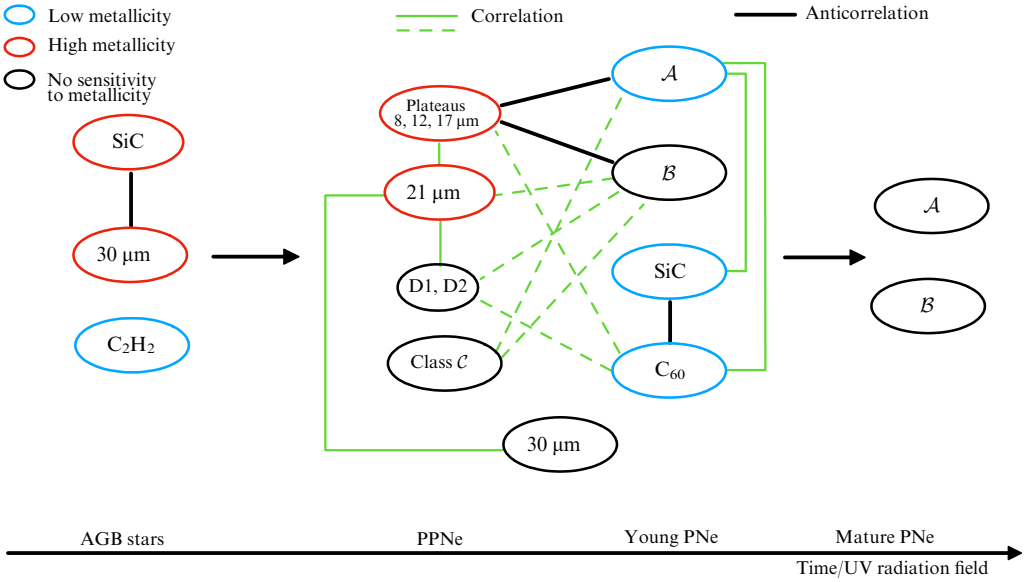

Figure 5. Schematic representation of observational features at different evolutionary stages from an AGB star to a mature PPN and relations between them, traced from observations. Features that are more frequent or more strongly manifested in high-metallicity objects are highlighted in red, and those in low-metallicity objects, in blue. Solid green lines indicate presence of a correlation between two features, and solid black lines indicate anticorrelations. Green dashed lines also indicate presence of correlations, but these correlations require additional study.

objects [28]. The bands associated with SiC (11.3 μm) and MgS (30 μm), on the contrary, are weaker in MC stars. At the subsequent stages of evolution, the feature at 30 μm is independent of metallicity [103], and the SiC feature, in contrast, is more pronounced in low-metallicity objects. While an anticorrelation between the intensities of the SiC and MgS bands is observed for AGB stars, this is not so for PPNe and PNe, but the intensity of the SiC band decreases as the radiation field hardness increases. Two scenarios have been proposed to explain this tendency: (1) destruction of carriers of this band [82] and (2) a decrease in the temperature of the band carriers due to the expansion of the envelope and increased separation from the central source [94]. We note that the processes of cooling and destruction of the 11.3 μm band carriers can occur simultaneously and exert a joint effect on the observed behavior of this band; the scenarios are therefore not mutually exclusive. The first scenario can be additionally used to support the hypothesis of the formation of fullerene molecules when SiC is exposed to UV radiation [120], because the intensity of the fullerene bands anticorrelates with the SiC band intensity [39]. The hypothesis of a relation between SiC and fullerenes seems very promising, because both these components are manifested to a greater extent in low-metallicity PPNe and PNe. Moreover, Otsuka et al. [39] showed that the average size of PAHs in C_{60}-PNe is smaller than in C_{60}-free PNe, and the spectra of C_{60}-PNe correspond to the $\mathcal{A}$ class, while Sloan et al. [66] note that most objects exhibiting the 'big 11' feature, i.e., presumably SiC particles, also belong to the $\mathcal{A}$ class. In addition, Sandstrom et al. [121] studied the IR characteristics of the MC ISM and came to the conclusion that PAHs in the MCs are on average smaller in size than in high-metallicity galaxies, which is related not to destruction but to formation features. Thus, there is circumstantial evidence that SiC and fullerenes may be related, but it is impossible to make definite conclusions about what kind of relation this is and at what stage of evolution it forms.

According to [66], most objects with the 21 μm feature (the coldest and youngest among the PPNe and PN) are divided into two different groups: those whose spectrum in the wavelength range of 11–14 μm corresponds to class D1, and those whose spectrum corresponds to class D2. Class D2 objects with the 21 μm feature have the 'bluest' colors, which indicates greater transparency than with other objects. As they evolve, PPNe branch into several types based on different features. One of the characteristic signs of the branching is the presence or absence of fullerenes. Recall that objects containing fullerenes are also 'bluer.' It is difficult to say whether objects with fullerenes and the feature at 21 μm have an evolutionary connection, but this possibility must be kept in mind. Objects with the feature at 21 μm correlate with the presence of continuums at 8, 12, and 17 μm. Apparently, the presence of such features reflects the 'immature' state of carbon particles, because these features appear only at the initial stages of the evolution of PPNe and PNe. Subsequently, simultaneously with the emergence of PAH/fullerene bands and an increase in their intensity, these features disappear or become less noticeable [91].

Objects of classes $\mathcal{C}$ and $\mathcal{D}$ are predecessors of class $\mathcal{A}$ and $\mathcal{B}$ ones, and, as the authors of [62] suggest, the particles responsible for the emergence of $\mathcal{C}$ and $\mathcal{D}$ spectra are something between small dust particles and freely flying PAHs, while particles in class $\mathcal{D}$ objects probably have a more pronounced aromatic structure, i.e., they represent a complex of PAHs. Jensen et al. [65] suggest that the $\mathcal{C}$ and $\mathcal{D}$ classes are different branches in the evolution of dust, while Carpentier et al. [61], in turn, point to a branching of the evolution of carbon particles into graphite-like (stacks of planar PAHs) and fullerene-like.

In class $\mathcal{B}$ objects, a band at 6.9 μm is found, and hence such objects most likely originate from class $\mathcal{D}$ objects. Shannon et al. [63] believe that class $\mathcal{A}$ objects are the next stage after class $\mathcal{B}$, appearing under the effect of destructive factors that make the average size of PAHs smaller. In any case, at the final stage of evolution, i.e., in the late PN stages

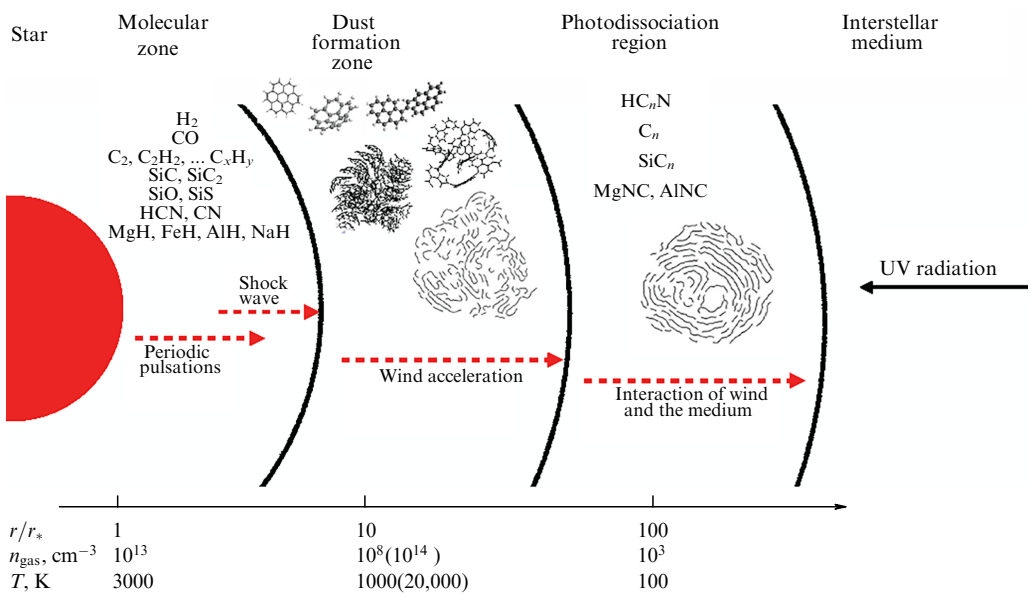

Figure 6. Schematic representation of the envelope of a carbon star at AGB stage.

and in the ISM, the IR spectra correspond to classes $\mathcal{A}$ or $\mathcal{B}$, and the entire diversity of IR features observed at the early evolution stages disappears.

3. Physical conditions in dust formation zones and in evolution of dust

Let us consider the conditions in the envelopes of AGB stars, at the late stages of which dust is formed, and the evolution of these stars ending with the PN stage. At the AGB star stage, helium and hydrogen are burning in the envelopes surrounding the stellar core. In Fig. 6, we schematically depict the stellar envelope divided into different zones by physical parameters and chemical composition. The figure shows the average values of the density ($n_{\rm gas}$) and temperature (T) of the gas, depending on the distance from the star, expressed in radii of the star ($r_\star$).[6]

The layer closest to the star (within several radii) is the molecule formation zone. Many molecules are formed there, including H_2, CO, C_2, C_2H_2, CN, HCN, SiC_2, SiS, and CS. The next zone is the dust formation zone, where solid macroparticles are formed: SiC, PAHs, amorphous carbon, and MgS. High-resolution observations together with theoretical calculations indicate that the dust formation zone is located at distances up to $\approx 20r_\star$ [122]. According to various estimates, the pressure in the stellar envelopes is in the range of $10^{-6}-10$ atm, the density is 10^8-10^{13} cm^{-3}, and the temperature is 500–2000 K [123–127]. Finally, the dust formation zone is followed by a large zone of a gradual transition to the ISM, where molecules and dust grains carried by the stellar wind are exposed to the UV radiation of the ISM, i.e., the PDR. This zone contains various carbon (C_n), polyyne (HC_nH), and cyanopolyyne chains (HC_nN), as well as SiC_n, MgCN, and other molecules that are products of photoreactions. The parent stars at the AGB stage are too cold to emit UV radiation, and hence such molecules are not formed in the layers closest to the star.

The dust formation zone is not uniform in its physical characteristics spatially and in time. The density and temperature decrease significantly when passing from the inner to the outer boundaries, and periodic shock waves caused by thermal pulsations of the star create unstable conditions. According to [23], when a shock wave passes, the temperature in the dust formation zone can reach $\approx 20{,}000$ K and the density can be greater than 10^{14} cm^{-3} (which is indicated in Fig. 6 in brackets for this zone); after that, cooling and adiabatic expansion occur. Shock waves can significantly affect dust formation. Their influence is confirmed by both theoretical studies [124] and observations, whence it follows that an increase in the duration and amplitude of pulsations of the star result in a greater amount of dust [117]. Although the dust (in particular, PAH molecules) formed at the shock wave front can be destroyed, it forms again during subsequent cooling. Shock waves and the associated dynamical processes can lead to the formation of clumps in the dust formation zone, which makes its characteristics even more heterogeneous [128].

Dust grains formed in the circumstellar envelope are exposed to radiation pressure from the star. The dust grains effectively absorb and scatter radiation and are pushed by this radiation into the outer layers. By transferring its momentum to gas particles, the dust entrains them. As a result of such processes, the stellar envelope is accelerated and mass is lost. Thermal pulsations, together with the acceleration of the envelope, lead to the detachment of the envelope from the star. The relation between the mass loss rate and various parameters of the star (mass, luminosity, temperature, excess carbon, and metallicity) is ambiguous [129]. One of the parameters influencing the mass loss rate is the effective temperature of the star, a decrease in which results in an increase in the mass loss rate [130, 131]. The defining parameters also include the mass and luminosity of the star [130]. Wachter et al. [130] suggest that the empirical correlation between the mass loss rate and the pulsation period arises from the period–luminosity coupling.

Wachter et al. [132] and Cummings et al. [133] concluded that the mass loss rate is virtually independent of the stellar metallicity. Moreover, Ventura et al. [134] concluded that the production rate of carbon dust is also independent of metallicity. At the same time, it was noted in [132] that, in

[6] The radius of the convective envelope is taken as the radius of the star.

contrast to comparable mass loss rates for solar metallicity, the LMC and the SMC, the stellar wind velocities of these objects of different metallicities are several times lower. Additionally, Mattsson et al. [24] hypothesize a threshold density for elements to condense into dust grains, below which dust formation is inefficient. Such theoretical conclusions are consistent with observational data. It has been noted that Sloan et al. [117] found an empirical relation between the mass loss rate and pulsation parameters, but not a relation to metallicity, except for extremely low-metallicity stars [28].

It is assumed in some models that the wind velocity is proportional to the relative carbon-to-oxygen excess and to the dust-to-gas mass ratio [112, 129]; however, this relation is not seen in observations. Höfner [128] believes that the wide range of parameters of observed stars, e.g., mass, age, and the initial chemical composition, leads to a blurring of the potential correlation, which may explain the absence of an observed correlation. However, given that the amount of formed dust is still smaller at low metallicity [135], the wind acceleration should occur more slowly.

When the burning of hydrogen and helium in layer sources ends, the star passes to the PPN stage. The layers in which the burning occurred start rapidly compressing, and $T_{\rm eff}$ gradually increases, the luminosity remaining unchanged. When a region of ionized hydrogen appears, the PPN passes into a PN. Most PNe are characterized by a 'two-shell' structure. The shells are formed as a result of different processes: ionization and stellar wind. Mellema [137] denotes these shells with the letters I and W (for ionization and wind). Figure 7 shows an image of the PN NGC 2022, where these shells and other zones characteristic of PNe are indicated. Most of the mass lost by the star during the AGB phase forms a dense outer envelope, also called a halo. This envelope moves away from the star at a velocity of $\sim$ 10–15 km s^{-1} [138]. Intense radiation from the central source penetrates the halo and ionizes the matter located there. At the boundary of interaction of radiation with intact matter, conditions for a shock wave and a corresponding shock front are created. Behind the shock front, there is a PDR where photons with an energy of less than 13.6 eV can penetrate, which can provoke the restructuring of carbon particles and numerous photoreactions. The shock front, and the photoionization front with it, move away from the star with time, expanding the inner H II region and also making the halo matter near the front denser and hotter. The interaction of radiation and halo matter determines the structure of young PNe.

As the central source evolves and is heated, a fast ($>$ 1000 km s^{-1}) but rarefied stellar wind begins to develop, accelerating due to the absorption and scattering of radiation by heavy elements [139]. A second shock wave is created that propagates to the interior of the H II region. Behind the front of this shock wave, as a result of thermalization of the energy of the powerful reverse shock wave, a very high temperature of $\sim 10^6$–10^7 K is reached, and the medium emits in the X-ray range. The thermal pressure in the H II region, on the one hand, pushes and accelerates matter to the outer regions, and, on the other hand, slows it down in the inner regions, which makes it denser at the shock wave front of the stellar wind. The PN then acquires the classic 'two-shell' structure. The 'two-shell' structure is relatively stable and disappears only during the cooling phase of the central source and recombination of PN matter or if the W-shell catches up with the I-shell [140]. The expansion velocity of the I-shell first increases rapidly, from $\approx$ 10 to $\approx$ 35 km s^{-1} at the PN stages

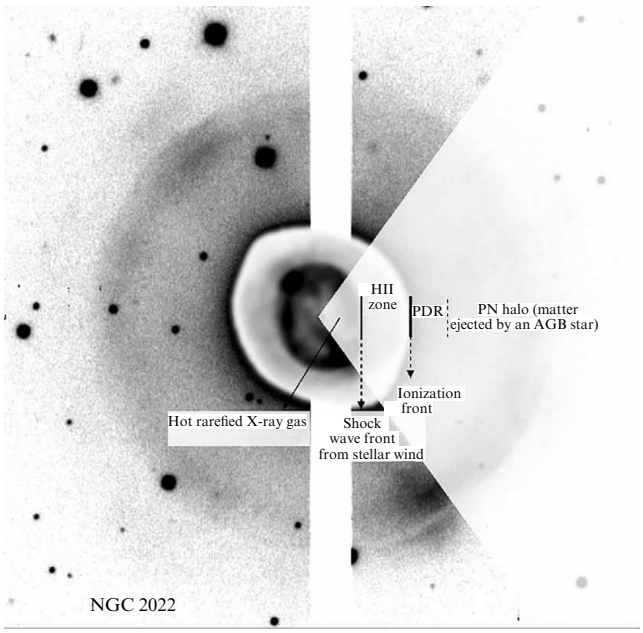

Figure 7. An [O III] image of the PN NGC 2022, showing the main regions characteristic of PNe. (Image taken with New Technology Telescope (NTT, Chile) in [136] and provided by Romano Corradi.)

up to $T_{\rm eff} \approx$ 50,000 K, and then more slowly, reaching 40–45 km s^{-1} at $T_{\rm eff} \approx$ 100,000 K [141]. The acceleration of the shell is apparently associated with the density gradient of matter in the halo, which implies that the matter ejection rate increased towards the end of the main mass loss stage. The expansion velocity of the W-shell, on the contrary, is almost constant in the beginning and is at the level of $<$ 10 km s^{-1}, and then starts increasing to 30–40 km s^{-1} due to the high pressure inside the shell, and can exceed the velocity of the I-shell [141]. In low-metallicity PNe, the expansion velocity of the outer I-shell is higher than for solar-metallicity PNe due to the higher electron density, while the expansion velocity of the inner W-shell, conversely, is lower, because the wind velocity is governed by the number of heavy elements [142].

4. Formation and evolution of carbon particles: modern theoretical concepts and experiments

4.1 From C_2H_2 to dust

The theory of the formation of carbon particles in stellar envelopes is in many respects borrowed from combustion theories which are based on experiments conducted under standard combustion conditions, although the conditions in stellar envelopes differ from those attainable in laboratories. In the gas of stellar envelopes, acetylene molecules predominate among small hydrocarbons, and hence these molecules are believed to be the first precursors of dust. The sequence of processes that leads to the formation of dust is approximately as follows: acetylene $\rightarrow$ benzene and polyynes $\rightarrow$ PAHs, nanobowls and fullerenes $\rightarrow$ PAH clusters $\rightarrow$ dust particles (soot). The stages of this sequence are described below, although alternative sequences of dust particle growth have been proposed in the literature [143].

4.1.1 Benzene ring. Acetylene molecules participate in a chain of chemical reactions leading to the formation of an aromatic

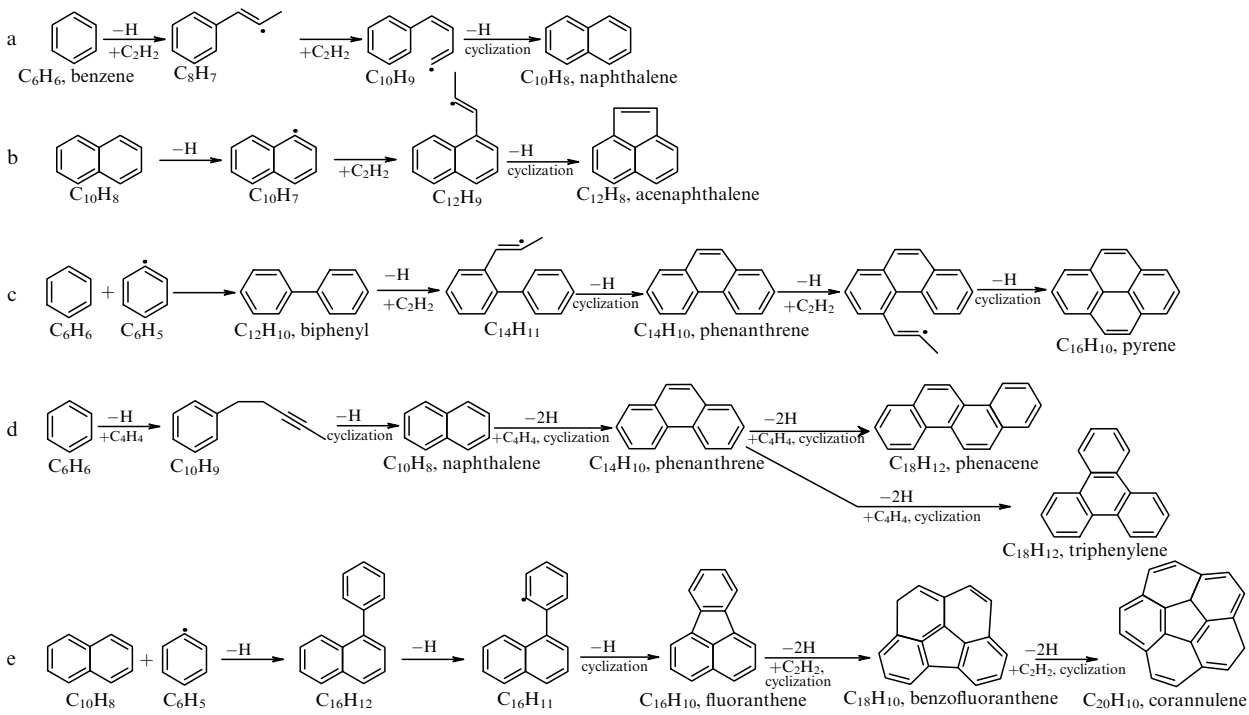

Figure 8. Examples of reaction chains leading to growth of PAHs: (a) HACA chain leading from benzene to naphthalene; (b) HACA chain leading from naphthalene to acenaphthalene; (c) HACA reaction chain leading from benzene and phenyl sequentially through biphenyl to phenanthrene and pyrene; (d) HAVA reaction chain leading from benzene through naphthalene to phenacene and triphenylene; (e) PAC reaction chain from naphthalene to fluoranthene, and then a HACA reaction chain to benzofluoranthene and corannulene.

ring, the benzene molecule C_6H_6. Several pathways have been proposed in the literature: recombination of propargyl ($C_3H_3^{\bullet}$) [144], a sequence of hydrogen abstraction and acetylene addition (HACA) reactions [145], and the reaction between 1,3-butadienyl C_4H_6 and acetylene [146]. All three reactions can occur simultaneously with varying efficiency both in stellar envelopes and in laboratory reactors, which leads to ambiguity in determining the main channel [147]. According to [124], the dominant one among these reactions in the envelopes of stars is the recombination of propargyl, but this mechanism, in contrast to HACA, almost has not been studied experimentally. In addition, other mechanisms of benzene formation have been proposed, for example, the formation of benzene rings on the surface of silicon carbide particles serving as a substrate and catalyst [148]. The PAH molecules themselves can be a catalyst for the formation of benzene. That is, having formed, a PAH molecule generates similar ones, which is the basis of carbocatalysis [149]. The formation of a benzene ring with the participation of catalysts is widespread in industries, but the analysis of these reactions in astrochemistry is a new direction, and the importance of catalytic reactions for astrochemistry is still underestimated, despite the high probability of their effective occurrence in the envelopes of stars and other objects of the ISM.

Cernicharo et al. [150] believe that benzene is formed not only in the stellar envelope at the AGB stage but also, and subsequently, in a PPN, when UV radiation appears and initiates many other chemical reactions. Among them is the polymerization of polyynes (HC_nH carbon chains), observed in PPNe along with benzene. Krestinin et al. [151], based on experiments with polyynes, believe that the combination of polyynes leads rather not to the formation of benzene rings but to the formation of PAHs and more complex macromolecules consisting of benzene/PAHs attached to each other by aliphatic bonds, and soot. Cherchneff [124] believes that such a mechanism can be effective for hydrogen-rich R CrB stars. In turn, Woods [152] proposed a model for the PPNe conditions, according to which benzene can appear as a result of a chain of ion–molecular reactions, including the dissociation of HCO^+, associative reactions of acetylene with $C_2H_3^+$ and $C_4H_3^+$, and others. It is assumed hereafter that aromatic molecules and dust are mainly formed at the AGB stage of a star.

4.1.2 PAHs with two or more rings. As soon as benzene rings appear in the medium, the processes of PAH growth and their clustering begin. The term 'growth' implies the formation of chemical bonds between the peripheral carbon atoms in the PAH molecule and other molecules (linear hydrocarbons or aromatic ones), resulting in an increase of the molecule in the plane. 'Clustering' means the process of combining two or more PAHs due to the formation of chemical or physical bonds between them. The combining can take place at any mutual arrangement of the PAHs, and this process therefore gives rise to three-dimensional structures [153].

The growth of PAHs can occur due to the HACA mechanism. There are variants of this mechanism, the classical one of which is the following chain (Fig. 8a):

- dehydrogenation of benzene and formation of phenyl ($C_6H_5^{\bullet}$);
- addition of acetylene;
- dehydrogenation;
- addition of acetylene;
- ring closure or, in other words, cyclization, accompanied by another dehydrogenation.

The further sequential addition of acetylene molecules should give rise to anthracene and phenanthrene molecules (both $C_{14}H_{10}$), but experiments and quantum mechanical

calculations show that the addition occurs as follows: a new ring is built on top of naphthalene and connects both of its rings, and the new ring is not six-membered, but five-membered (Fig. 8b) [154, 155]. Such a molecule is called acenaphthalene ($C_{12}H_8$). Five-membered rings subsequently result in a curvature of the PAH plane, and therefore the classical HACA scenario does not lead to the formation of large planar PAHs.

An alternative pathway for the formation of naphthalene is the condensation of two phenyls and the formation of biphenyl and subsequent dehydrogenation, the addition of acetylene, and cyclization (Fig. 8c). In this case, the third ring is six-membered, and the final molecule is phenanthrene. Subsequent dehydrogenation and the addition of acetylene lead to a four-ring molecule, pyrene ($C_{16}H_{10}$). This pathway has been confirmed both by quantum mechanical calculations and by experiment [156, 157]. In essence, this mechanism can be attributed to the HACA mechanism, because the same sequence of reactions occurs.

A mechanism similar to HACA is the HAVA (hydrogen abstraction — vinylacetylene addition) mechanism, in which a vinylacetylene molecule (C_4H_4) is added to benzene after the abstraction of a hydrogen atom [158]. Initially, these two molecules form a van der Waals complex, which subsequently undergoes isomerization, becomes stable, and forms a naphthalene molecule (Fig. 8d). Because the formation of the phenyl–vinylacetylene complex occurs without a barrier, this mechanism operates even at low temperatures, typical of molecular clouds [158]. Thus, HAVA is a more universal mechanism than HACA. Moreover, unlike HACA, the HAVA mechanism can lead to a further growth of PAHs with six-membered rings, i.e., the formation of naphthalene can be followed by the synthesis of anthracene, phenanthrene, phenacene ($C_{18}H_{12}$), triphenylene ($C_{18}H_{12}$), helicene ($C_{18}H_{12}$), and other PAHs [157, 159]. In Fig. 8d, the pathways to phenacene and triphenylene are shown. Experiments tracking the considered mechanism were conducted in reactors at both high temperatures corresponding to the envelopes of AGB stars [160] and extremely low temperatures, around 10 K [158].

A mechanism competing with HACA and HAVA is PAC (phenyl addition–dehydroCyclization), which includes successive reactions of phenyl addition, dehydrogenation, and aromatic ring closure [161, 162]. Phenyl can attach to two carbon atoms of the biphenyl molecule, and, after several dehydrogenation reactions, a new ring closes in the center between the three original ones, and a triphenylene molecule is formed ($C_{18}H_{12}$). If phenyl attaches to a naphthalene molecule, the same sequence of reactions leads to the formation of fluoranthene ($C_{16}H_{10}$), which has a five-membered central ring (Fig. 8e). Both pathways have been tracked in experiment [161, 163]. If the triphenylene molecule is a precursor of planar PAHs, then the fluoranthene molecule leads to the formation of volume molecules and particles, including fullerene molecules, which is discussed below. It should be noted that the factors determining which of the mechanisms, HACA, HAVA, or PAC, dominates in the dust formation zone are unknown.

The considered reactions promote the growth of PAHs from smaller components (the so-called bottom-up mechanism), whereas PAHs can be formed in the ISM by the destruction or transformation of larger particles (the top-down mechanism). Merino et al. [125] conducted an experiment in which the surface of silicon carbide coated with a thin layer of graphite was hit with a hydrogen beam under conditions simulating the envelope of an AGB star. As a result, benzene and PAH molecules were detected, whence it was concluded that not only the benzene ring (as in [148]) but also PAHs are formed on the SiC surface. Scott et al. [34] detected PAHs among the dissociation products of HAC particles. Thus, top-down mechanisms can be considered an additional source of PAHs.

4.1.3 Fullerenes. Fullerene molecules are often present among the combustion products of hydrocarbons along with PAHs and soot. It was noted in [164, 165] that fullerenes are more likely to form at low pressures. Several theories have been put forward in the literature on how and under what conditions these molecules are formed, but not all of them are applicable to space conditions. As in the case of PAHs, the formation mechanisms can be divided into two categories: bottom-up and top-down.

We start with the bottom-up mechanisms. In industry, fullerenes are obtained from carbon vapor at high temperatures. Carbon vapor can be produced in different ways: by heating and evaporation of graphite rods, by laser ablation of graphite plates, by electric arc discharge between graphite electrodes, or by combustion of hydrocarbons. In all these methods, the fullerenes are assumed to be assembled from small components, but how exactly the assembly process occurs is not determined. Dunk et al. [166] proposed an assembly mechanism called 'closed network growth' (CNG). According to this mechanism, the smallest fullerenes ($N_C = 24, 28$) appear first, and then these fullerenes grow by adding atomic carbon and diatomic carbon molecules. In essence, in other words, the fullerenes formed first catalyze the growth of higher fullerenes. In subsequent studies, Dunk et al. [167] showed that such a process should occur in the conditions of stellar envelopes in the presence of hydrogen and/or oxygen. Moreover, they showed that, in addition to pure fullerenes, there is a high probability of metallofullerene formation in stellar envelopes and in supernova remnants.

In [166, 167], only a general concept was proposed, whereas a detailed elaboration of the chain of chemical reactions occurring during the assembly of fullerenes is needed. It has already been shown above that the PAC mechanism can lead to the formation of a fluoranthene molecule ($C_{16}H_{10}$). Fluoranthene can grow to coranulene ($C_{20}H_{10}$) via the HACA mechanism, i.e., as a result of a sequence of reactions of hydrogen abstraction and acetylene addition (Fig. 8e). This chain of reactions has been studied both theoretically and experimentally [168]. In [169], a subsequent path from coranulene to the nanobowl $C_{40}H_{10}$ was demonstrated numerically. This nanobowl has a hemispherical shape, is of the same structure and geometry as the fullerene C_{60} molecule, and makes up $2/3$ of C_{60}. The authors of [169] believe that the nanobowl is a fullerene precursor. The main mechanism of $C_{20}H_{10}$ growth to $C_{40}H_{10}$ is HAVA. First, a pentacoranulene molecule $C_{40}H_{20}$ forms due to five successive reactions of vinylacetylene molecule addition, accompanied by dehydrogenation, and then the pentacoranulene molecule undergoes several cycles of dehydrogenation and cyclization, resulting in the formation of a nanobowl $C_{40}H_{10}$. Thus, a step-by-step scenario of the bottom-up mechanism of the formation of the fullerene C_{60} precursor is presented in [169]; this scenario can be realized in envelopes of carbon AGB stars, but its efficiency has yet to be assessed.

Homann [170] proposed a slightly different scenario of fullerene formation for low-pressure flames. According to this mechanism, first, two planar PAHs are cross-linked due to the formation of one bond between two peripheral rings. Next, a second bond is formed between these rings and a new ring is closed, which becomes five-membered. Then, a sequential chain of HACA and cyclodehydrogenation reactions occurs, whereby new rings are formed, mainly five-membered. An increase in the number of five-membered rings leads to a stronger curvature of the molecule and its gradual folding into a fullerene.

In astronomical studies, the idea of alternative, top-down, mechanisms of fullerene formation has become very popular. This is important for expanding the potential sources of fullerenes and modeling the evolution of carbon particles in stellar envelopes and beyond. Top-down mechanisms are supported primarily by experiments in which fullerenes are formed as a result of the destruction of larger particles. In [171], a graphene monolayer exposed to irradiation from an electron gun was used as such particles. This process was monitored using an electron microscope. The images showed changes in the structure of the graphene layer and its transformation into fullerene in real time. In [172], PAH molecules $C_{66}H_{26}$ and $C_{78}H_{26}$ irradiated with a UV laser were used instead of graphene. The dissociation products were detected using a mass spectrometer, and among the products were fullerene molecules C_{60} and C_{70}. In the experiment in [34], HAC films were exposed to external influence (UV radiation), and a mass spectrometer recorded many different PAHs (naphthalene, $C_{10}H_8$, anthracene, $C_{14}H_{10}$, etc.) and fullerenes C_{60} and C_{70} among the dissociation products.

Based on the results of these experiments, several scenarios for the formation of fullerenes were put forward and several models were developed: Micelotta et al. [173] proposed a model for the formation of fullerenes from HAC; models for the formation of fullerenes from PAHs were developed in [174, 175]. However, it is likely that the bottom-up and top-down mechanisms coexist in space objects, with a varying contribution from each, depending on the specific physical conditions.

4.1.4 Macroparticles (dust). The next stage after the formation and growth of PAHs and/or fullerenes is their clustering and the formation of macroparticles. During the first stages of combustion, the following particles can be observed under various conditions: (1) polyynes, positively charged and neutral (with the diameter d of the order of 1 nm); (2) PAHs and graphenes in a wide range of sizes, also positively charged and neutral ($d \sim 1$ nm); (3) fullerenes ($d \sim 1$ nm); (4) nanosize soot seeds or PAH clusters ($d \sim 1$–6 nm), which lack a regular structure; subsequently, these seeds become the nuclei of soot particles and, probably, also interstellar dust; (5) partially mature particles ($d \sim 1$–6 nm) that contain layered graphite-like structures; and (6) primary nanoparticles with a mature, most regular structure ($d > 6$ nm) [143]. By macroparticles, we understand particles from item 4 and further. It should be noted that the hydrogen-to-carbon ratio reaches high values in the most immature particles (item 4) and is about 0.7, and then this ratio decreases as the soot matures [143].

In the formation of soot, PAHs are preferable to aliphatic hydrocarbons as precursors. This was found by measuring the soot yield at different fuel compositions [176]. While the identification of large PAHs was difficult, it was believed that only PAHs consisting of just a few (2 to 5) aromatic rings participate in soot formation [177], but, with the development of technological capabilities, it became obvious that large PAHs up to 80–100 carbon atoms are present in the combustion process [178], and all of them can form clusters, although clusters produced from larger PAHs may take more time to be formed and are therefore more rare [179]. In contrast to the formation of PAHs, modeling and experimental monitoring of their clustering process are more difficult, despite a large number of studies in this field [180–182]. It remains unclear exactly how the PAH clusters, or, in other words, primary soot seeds, are formed. Dimers and clusters formed by physical (van der Waals) bonds alone are unstable, and the rate of the reverse reaction exceeds the rate of the forward reaction.

Curved PAHs are polarized, and hence compounds involving them have higher binding energies than those with planar PAHs. If curved PAHs are present or even prevalent in the environment, the process of their clustering can be dominant in dust growth [187]. However, even in that case, the soot formation rate is too low to explain the amount of soot formed.

Because the rates of physical clustering and soot growth due to chemical reactions, for example, via the HACA mechanism, do not reach the required values [143, 188], the question of a combination of these processes began to be investigated. It is assumed that, during the formation of a physical PAH cluster, a chemical bridge forms between the PAHs, which stabilizes this cluster.

Compact PAHs (e.g., coronene) formed during combustion are not chemically active in the neutral form, but reactions between their radicals can be very effective. PAHs that have lost one hydrogen atom become highly reactive according to quantum mechanical calculations [183]. These PAHs can form dimers both with the same radicals and with nonradical PAHs [184, 185] (Fig. 9a). PAHs with five-membered rings are more active in forming dimers than ordinary PAHs [186]. Frenklach and Mebel [182] proposed an 'E-bridge,' which is made of two bonds between two free peripheral carbon atoms in a PAH; given such a bridge, the presence of a peripheral five-membered ring is necessary. Aliphatic bonds between aromatic molecules can act as a bridge [189–191], which is considered the option closest to the case of stellar envelopes. PAHs with alkyl groups and aliphatic bridges have been detected experimentally both in combustion reactors under atmospheric pressure [192] and in astrochemical experiments, which revealed the presence of both aromatic and aliphatic bonds in the formed particles [193]. With this formation of PAH clusters, the resulting particles are characterized by a high H/C ratio, which is important for stellar envelopes because of their high hydrogen content. It is assumed that the leading role in the formation of aliphatic bridges is played by methyl groups attached to PAHs; the detachment of a hydrogen atom from them leads to the formation of an active radical. PAH molecules can also be linked via acetylene molecules and polyacetylene chains [194, 195]. We also note that the stability of aliphatic PAHs increases if the PAHs have five-membered rings [196].

According to [182], the 'E-bridge' is kinetically stable, unlike single aliphatic bridges and other types of compounds (for example, zigzag ones); nevertheless, aliphatic bridges can probably survive under the conditions of stellar envelopes. A model of the formation and evolution of nanoscale arophatic clusters, which can be considered as PAH clusters in which

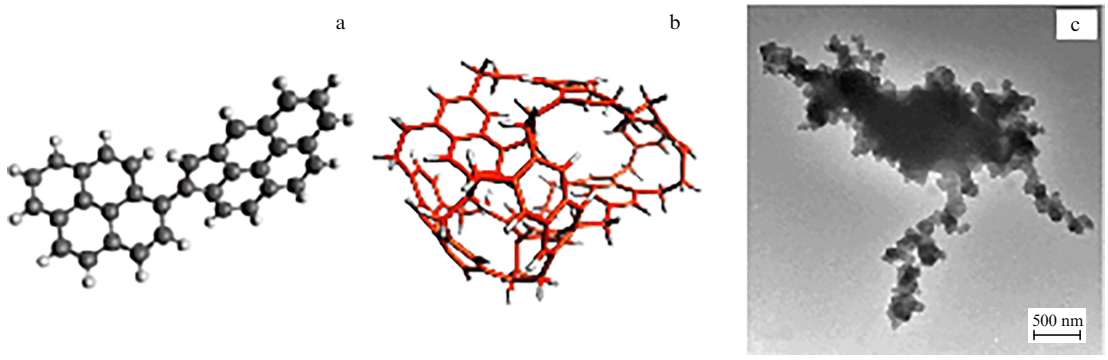

Figure 9. (a) Simulated image of a PAH cluster formed by an aliphatic bridge. (Reprinted with permission from [191]. Copyright American Chemical Society, 2020.) (b) Simulated image of an arophatic particle. (Illustration taken from [173] with permission from the AAS.) (c) Microscopic image of a soot particle. (Taken from [199] with permission from the AGU.)

PAHs are connected by aliphatic bonds (Fig. 9b), was presented in [173]. The authors hypothesize that such particles serve as precursors for interstellar fullerenes, because, when interacting with UV radiation, they lose the weakest aliphatic bonds and gradually acquire a closed fullerene-like shape. A more extensive model, based on the same idea of the formation of primary soot particles from PAHs by their connection with aliphatic bonds, was presented by Jones in a series of studies [59, 197, 198].

The resulting dust grains, according to the Jones and Micelotta models [59, 173, 197, 198], have high H/C ratios and an sp^3/sp^2 bond hybridization. These grains then evolve under the influence of the UV radiation field in PPNe and PNe. Their structure changes from a chaotic amorphous state with a small number of aromatic islands to a more ordered arrangement with predominantly aromatic bonds. This transition is monitored by the ratio of the band intensities at 3.3 and 3.4 μm [58]. During this process, various fragments can separate from the grains, including freely flying PAHs and fullerenes [34]. Despite a common formation mechanism, the building blocks of particles at low and solar metallicities would most likely be different. The ratio between the number of nonplanar (five-membered) PAHs and planar (six-membered) PAHs is likely to be higher in the former case, which mainly leads to the formation of fullerenes possible.

After the formation of primary soot particles with a nearly spherical shape, the process of aggregation and coagulation of these particles begins, resulting in the formation of nonspherical conglomerates. The efficiency of this process depends largely on the particle collision rate, i.e., on their concentration. Consequently, under the conditions of stellar envelopes, it probably does not proceed as efficiently as in combustion reactors, but, as noted in [87], dust particles must be asymmetric to explain the observational characteristics in PNe, and it is therefore possible that large dust particles are asymmetric conglomerates of primary soot particles with a high degree of fractality, similar to those observed in laboratories (Fig. 9c).

4.2 Effect of oxygen on formation and evolution of polycyclic aromatic hydrocarbons, fullerenes, and dust

Determining the factors that significantly affect the final products obtained in experiments is important for establishing the cause of the nonuniform distribution of fullerenes and PAHs in PPNe and PNe with different characteristics, in particular, metallicity. According to the results of experiments, factors such as temperature, pressure, and the initial gas composition affect both the number/amount of PAHs, fullerenes, and dust, and the structure of dust (see Section 5 and [164, 165, 200]). As regards the combustion process, one of the key elements in the gas composition is oxygen. In experimental studies, a significant effect of oxygen on the combustion process and the final products, including the formation of fullerene molecules, has been repeatedly noted [165, 201]. In chemical modeling of the envelopes of AGB stars, it is generally assumed that all oxygen is locked in CO, and therefore it does not participate in carbon chemistry reactions [202]. However, Cherchneff [23] believes that atomic oxygen can appear in the gas due to collisional dissociation of CO during the passage of periodic shock waves. In some studies (see, e.g., [23, 203]), oxygen is included in the network of chemical reactions of the envelope models of AGB stars, which then allows explaining the formation of water molecules observed under these conditions. It is possible that, besides the water formation reactions, oxygen also participates in carbon chemistry reactions that give rise to PAHs, fullerenes, and dust. In the overwhelming majority of astrochemical experiments, the influence of oxygen is not discussed either, although its presence among the reactants is possible. As an exception, we note the experiments in [60, 61] (see Section 5), which indicate that oxygen is not included in the final composition of soot. In this section, we discuss the influence of oxygen on the formation of carbon particles in more detail in order to emphasize its potentially significant role in this process in the envelopes of AGB stars, whereas, in Section 5, which is devoted to astrochemical experiments, the role of oxygen is not considered.

The function of oxygen in combustion of hydrocarbons has not been established unambiguously. The diverse data on its influence available in the literature are evidence of the complexity of this influence. First, oxygen affects the formation of PAHs. In [182], it was concluded that, when combustion reactors are pumped with oxygen, PAHs are oxidized and their sizes decrease. In [204], it was emphasized that taking oxygen chemistry into account is necessary to correctly describe the results of experiments with its addition. In the absence of oxygen, PAH growth occurs due to the addition of acetylene (the HACA mechanism), but, in the presence of oxygen, the addition of acetylene competes with the addition of oxygen. The addition of oxygen leads to the formation of heterogeneous (oxygen-containing) five-mem-

bered rings in PAHs, which can participate in chemical reactions differently from homogeneous PAHs. The authors of [204] suggest that curved PAHs (with five-membered rings) are more likely to form dimers than their flat counterparts. According to the authors, the structure and shape of PAHs are more important factors for dimerization and further clustering than their size. Liu et al. [205], on the contrary, argue that oxygen-containing PAHs can significantly affect the chemistry of PAHs, but not the process of initiation of clustering and soot formation. Frenklach et al. [188] share the same opinion and believe that oxygen cannot be a key element for the PAH clustering process.

Oxygen may not be key for the initiation of the PAH clustering process, but it has a significant effect on the amount and structure of the formed soot. In [206], it was shown experimentally that the addition of oxygen to fuel in moderate quantities results in soot formation starting at lower temperatures ($\lesssim 2000$ K) compared to pyrolysis, whereas, at higher temperatures, the addition of oxygen suppresses soot formation. The effect of oxygen was especially strong in acetylene gas. An increase in the amount of soot and its faster formation with the addition of oxygen to the fuel were also observed in [207].

In the experiment conducted in [208], smaller particles and a smaller amount of soot were formed with the addition of oxygen, although the number of precursors of aromatic molecules (e.g., acetylene) and small aromatic PAHs was greater. Thus, a larger amount of acetylene and higher number of small PAHs does not guarantee a greater number of large particles.

Furthermore, it was shown experimentally in [209] that adding oxygen up to a certain level leads to an increase in the amount of soot, but then, on the contrary, suppresses soot formation. In [210], the nonmonotonicity of the dependence of the soot yield on the amount of added oxygen was also tracked; first, an increase is observed, which is followed by a decline. The authors believe that the addition of oxygen disrupts the balance between the PAH growth and soot formation processes, and unexpected reverse effects can occur in these processes at certain oxygen concentrations. We also noted that the addition of oxygen to the fuel leads to a richer composition of its decay products, i.e., various soot precursors, which increases the versatility of soot formation pathways [210].

Let us consider how oxygen can affect the synthesis of fullerenes. Baum et al. [164] demonstrated that the number of synthesized fullerenes depends on the amount of oxygen: at $C/O \approx 1$, the maximum number of C_{60} fullerenes is reached, and with a change in C/O in one direction or another, the number of fullerenes decreases. Small PAHs with $N_C \lesssim 30$ carbon atoms behave similarly, while the number of larger PAHs, on the contrary, increases. A similar anticorrelation between the number of PAHs and fullerene/curved structures was observed in the experiments in [165], where the structure of carbon particles changed, depending on the flame height: initially, curved molecules and fullerene-like soot were formed, but after reaching a peak in the number of fullerenes, planar molecules began to form instead of curved ones. The authors of [165] believe that, with a higher amount of oxygen, oxidation of fullerenes occurs, which negatively affects their number but favors the growth of PAHs due to oxidation and the release of peripheral bonds for the addition of acetylene. In addition, they established experimentally that fullerenes are formed more efficiently at lower pressures, and their absolute number, like the amount of soot, can decrease, but their number relative to soot increases.

Finally, oxygen can have different effects on combustion products, depending on whether it is present in atomic or molecular form. According to [201], an increase in the level of atomic oxygen in the initial gas leads to the formation of planar structures, while, in the presence of molecular oxygen, the number of fullerenes and amount of fullerene-like soot increase. At minimum amounts of atomic and molecular oxygen, curved structures are observed; with an increase in the amount of atomic oxygen, until a certain level is reached, planar PAHs dominate, and these PAHs are large. But, with a further increase in the amount of atomic oxygen, the size of the resulting PAHs decreases.

Summarizing the results of the experiments, we can conclude that (1) the oxygen abundance affects the size, shape, and number of the resulting PAHs; (2) the oxygen abundance determines the appearance of curved molecules and fullerenes; (3) the dependence of the number of formed soot particles is nonmonotonic: on the one hand, small quantities of oxygen favor the formation of soot, but, on the other hand, when a certain level is reached, the formation of soot is suppressed. The results of the described experiments cannot be directly adapted to the conditions of the dust formation zone, but they allow arguing that oxygen plays an important role in the formation of carbon particles in it, as it does in the laboratory. Therefore, theoretical and experimental studies of the formation of carbon particles are needed, in view of the function of oxygen as one of the factors influencing the final products observed in AGB stars, PPNe, and PNe, as well as later in the ISM.

In this section, the role of oxygen was considered, but other chemical elements can also affect the formation of PAHs, fullerenes, and dust. Metal catalysts, widely used in industry, are present in the envelopes of AGB stars, but their function is not considered in astrochemistry, whereas, for example, nickel promotes the twisting of planar PAHs into fullerenes according to [211]. Considering the moderate relative number of heavy elements, it is doubtful that they can play a significant role in the chemical evolution of carbon particles and other molecules. However, even single atoms inside carbon particles can be important, as shown by studies of single-atom catalysis [212, 213], and therefore the assessment of the influence of catalysts on the formation and growth of carbon particles requires no less attention than the assessment of the influence of oxygen.

5. Astrochemical experimental studies of interstellar dust analogues

5.1 Laboratory synthesis of interstellar dust analogues

The conditions in stellar envelopes can be compared with combustion reactors, the difference being that the main chemical element in the envelopes is hydrogen, and the density and pressure are lower than normal and than those usually maintained in laboratory reactors. Namely these factors — the chemical composition and pressure of the gas — are critically important for the structure of the particles formed. For example, it was noted in [214] that an increase in the hydrogen abundance leads to an increase in PAHs among the products, while the fraction of fullerenes decreases, and hence hydrogen-rich envelopes do not favor the formation of fullerenes. The defining role in the formation

of a particular structure is played by pressure: at its elevated values, a regular graphite structure is formed, and at extremely high values, a diamond-like structure is formed [215–217]. Pressure also affects the size of the particles formed. For example, when the pressure was reduced from 10 to 3 atm, the diameter of the primary soot particles formed decreased from 47 to 17 nm [218]. Temperature is an equally important parameter [219].

As already mentioned above, the pressure in stellar envelopes is $10^{-6}-10$ atm, the density is $10^{8}-10^{13}$ cm^{-3}, and the temperature is 500–2000 K [123–127]. To obtain astrochemically relevant results, specialized experiments are conducted in which conditions are created that are as close to the those of stellar envelopes as possible and are aimed at producing interstellar dust analogues (IDAs). To date, many different techniques have been used, which are listed in [61] and in the supplementary material to [220]. This list includes laser ablation, combustion, pyrolysis, dusty plasma, and gas condensation. Below, we discuss the results of astrochemical experiments using various techniques.

Kovačević et al. [221] conducted an experiment to study the formation of dust in a reactor during the occurrence of a radio-frequency discharge in a gas of acetylene, argon, nitrogen, or oxygen. The pressure in the reactor was set at 10^{-4} atm; the temperature was at the room value (about 290–300 K). Particles were formed in the resulting plasma, in the IR spectra of which aliphatic bands were present at 3.4, 6.9, and 7.3 μm. It is assumed that the growth of particles occurred due to the polymerization of low-atomic hydrocarbons ($C_{2n}H_m$), including benzene rings.

In [222], experiments were conducted with laser ablation and laser pyrolysis of carbon materials at different pressure and temperature values. These experiments can be divided into two categories: high-temperature ones with $T > 3500$ K and a pressure of $10^{-3}-10^{-2}$ atm, and low-temperature ones with $T \approx 1000$–1700 K and a pressure of ≈ 0.7 atm. Graphite electrodes (for ablation) and hydrocarbons (C_2H_2, C_2H_4, and C_6H_6) were used as precursors. The products of laser ablation and laser pyrolysis were deposited on a substrate and analyzed using electron and mass spectroscopy, chromatographic methods, and a spectrometer. In the high-temperature regime, small (several-nanometer) particles of fullerene-like soot were obtained, whose structure is based on spherical molecules linked by aliphatic or van der Waals bonds. In the low-temperature regime, larger particles of graphite-like soot (several tens of nanometers) were obtained, along with a number of different PAHs. The authors assume that the first regime corresponds to the remnants of supernovae or Wolf–Rayet stars, and the low-temperature mode, to the envelopes of AGB stars. Indeed, in the dust condensation zone around AGB stars, the temperature does not exceed 2000 K on average, but, as was shown in [23], it can reach 20,000 K during the passage of shock waves, and hence it is possible for fullerenes and fullerene-like soot to be formed precisely at the moments of shock wave passage, and for PAHs and graphite-like soot to be formed at other times.

Biennier et al. [223] conducted an experiment on the pyrolysis of acetylene gas. The pressure and temperature in the chamber were maintained at 10^{-5} atm and 1800 K. The obtained particles were complexes of aromatic rings linked by aliphatic bonds. Despite the predominantly amorphous structure, graphite inclusions consisting of several graphene layers were found in the particles. Both aromatic and aliphatic bands were observed in the IR spectra of these particles. The authors suggest that the obtained particles are an intermediate stage in the evolution of dust on the way to aromatization.

An example of experiments on hydrocarbon combustion under astrophysical conditions is provided by the one in [60]. The temperature was about 2000 K and the pressure from 2×10^{-2} to 10^{-1} atm. Unsaturated hydrocarbons (C_2H_2, C_2H_4, and C_3H_6) were used as precursors; they were mixed with oxygen in such a proportion that the C/O ratio ranged from 0.5 to 2. After the combustion reactor, the gas entered the precipitation chamber with a pressure about 10^{-3} atm and room temperature. The combustion products were deposited on a substrate, and IR spectroscopy of the resulting IDA (more than 50 different samples) was applied. The main results in [60] are as follows: (1) acetylene is the most suitable precursor for dust formation, and (2) the ratio between the intensities of the bands at 3.3 and 3.4 μm, i.e., between the number of aromatic and aliphatic bonds, definitely correlates with the position of the band at 6.2 μm. The central wavelength of the band at 6.2 μm was observed at ≈ 6.3 μm for the least aromatic samples and was shifted to 6.2 μm for the most aromatic ones. Although no structural analysis of the samples was performed in [60], the IR spectra indicate that the particles obtained are a mixture of aromatic molecules linked by aliphatic bonds. This experiment is consistent with the assumption that class $\mathcal{C}$ objects contain mainly dust particles with a large fraction of aliphatic bonds, while class $\mathcal{A}$ and $\mathcal{B}$ objects, on the contrary, contain dust particles with predominantly aromatic bonds. The authors note that the presence of oxygen in the initial gas mixture did not affect the final spectra, i.e., bands corresponding to bonds between carbon and oxygen were hardly observed.

Carpentier et al. [61] performed a similar experiment on the same setup as in [60], varying the initial mixture composition (C_2H_4/C_3H_6), carbon-to-oxygen ratio (C/O = 1.1, 1.4, and 1.6), and pressure (from $\approx 10^{-2}$ to $\approx 8 \times 10^{-2}$ atm). Three samples of IDA were obtained, which can be compared to three different types/stages of objects. According to high-resolution images (Fig. 10), these samples are as follows. (1) Sample 1 is a material with the least number of curved and tortuous substructures and the largest number of planar aromatic molecules, poorly connected to each other; the ratio $sp^3/sp^2 \approx 0.1$ is low. (2) Sample 3 is a material with the largest number of nonplanar, tortuous, and curved aromatic substructures, well connected to each other by aliphatic bridges; the substructures have a predominantly curved or quasi-spherical shape and there are many defects in the form of non-six-membered rings in the aromatic molecules that make up the substructure or on the periphery of these molecules, where they are connected by aliphatic bridges; and the ratio $sp^3/sp^2 \approx 9$ is high. (3) Sample 2 is a material with intermediate characteristics between Sample 1 and Sample 3. We note that Sample 1 particles were obtained at the maximum C/O value equal to 1.6, and Sample 3, at the minimum value equal to 1.1. It is noted in [61] that, in the process of dust formation, the evolutionary path apparently branches into the paths leading to PAHs and to fullerenes. The 'fullerene' path can then eventually lead to the formation of not only fullerenes but also particles with spectral properties of classes $\mathcal{A}$ and $\mathcal{B}$ as a result of transformations and the formation/growth of planar PAHs on the surface. In [222], such branching occurred, depending on the temperature, but it was shown in [61] that branching can occur when the gas

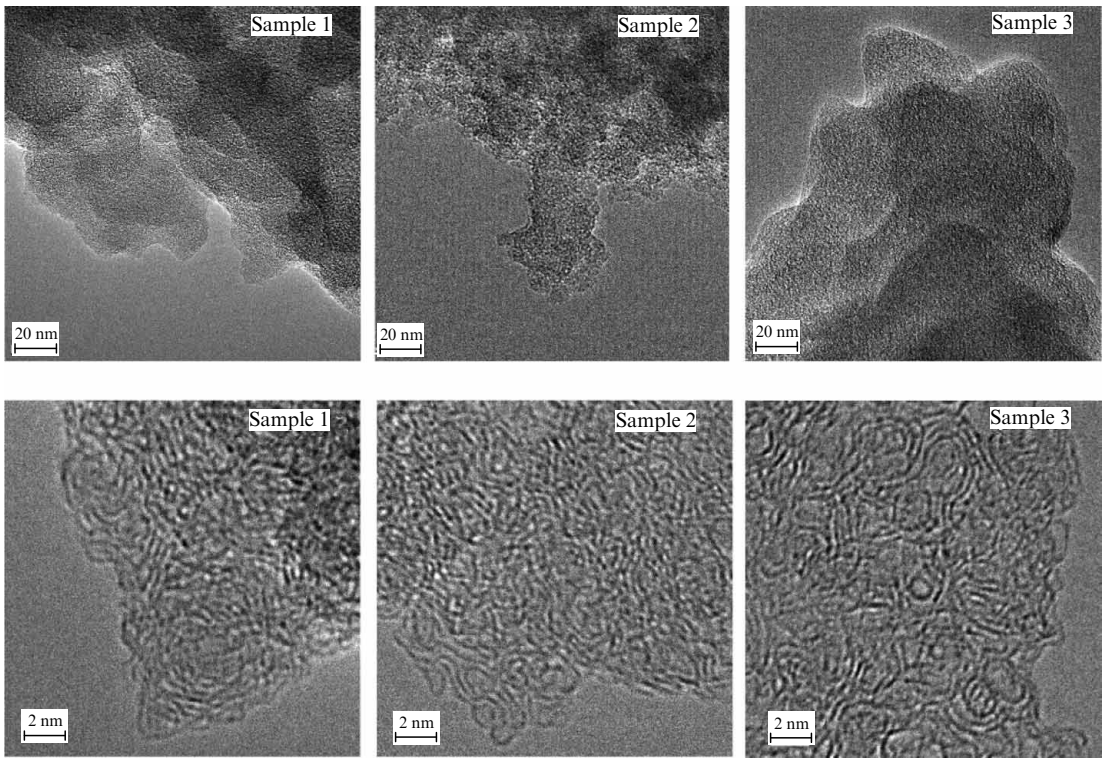

Figure 10. High-resolution electron microscope images of IDA samples. (Figure taken from [61] with permission from A&A.)

composition and pressure vary. The difference between the samples lies in the tortuosity and curvature of the molecules and in their connections to each other. We have noted that dimers and clusters of curved molecules are more stable, and the bonds in these clusters have different characteristics. Such a material can probably be more resistant to external effects. The structure of the formed particles is irregular, but not purely amorphous, because it consists of aromatic molecules. The authors of [61] note that, during the formation of dust, a separate branch with particles of amorphous carbon must also exist.

The results of an experiment at the COSmIC facility,[7] designed specifically to simulate the processes of formation and growth of IDAs, are presented in [224]. In the experiment, a pulsed gas discharge was created in a prepared gas mixture with argon as a carrier gas, resulting in the generation of a supersonic plasma jet with parameters close to the astrophysical ones. Various carbon molecules and particles were formed in this jet. The formed particles were registered and identified using a high-resolution spectrometer and time-of-flight mass spectroscopy. Various mixtures were used as initial ones, including mixtures of alkanes, alkynes, alkenes, monocyclic aromatic molecules (e.g., benzene), PAHs, and combinations of such mixtures. As a result, it turns out that, first, the final products differ greatly if the precursors are different, and second, particle growth is observed only in the case of mixtures of unsaturated hydrocarbons and monocyclic aromatic rings, while, when using mixtures of PAHs (e.g., naphthalene), molecular growth of particles did not occur. Thus, it was demonstrated experimentally that particles grow due to chain elongation, the formation of aromatics, and the interaction of the smallest aromatic molecules and unsaturated hydrocarbons. Small hydrocarbons initiate reactions of carbon particle growth, while PAHs can serve as building blocks for clustering but do not initiate their growth.

Recently, the Stardust facility [220] was built, where, in contrast to combustion or gas discharge experiments, astrophysical conditions of the dust condensation zone are directly produced. This facility consists of several modules aimed at studying different conditions. The module for studying the envelopes of AGB stars contains four chambers connected in series, simulating the path of atoms/molecules from the inner to the outer regions of the envelope: (1) a chamber where the initial gas mixture is injected and where the aggregation and growth of molecules and particles begin; (2) a diagnostic chamber, whose contents are measured; (3) a furnace chamber, where temperatures comparable to that in the dust formation zone are attained; (4) an acceleration chamber, where the formed particles are accelerated similarly to how this occurs in the envelopes of AGB stars. The chemical composition in each chamber can be controlled and the required ratios between the elements can be created. To date, the Stardust setup is undoubtedly the closest to astrophysical conditions, and the results obtained there are of particular interest.

In [220], the results of an experiment at the Stardust facility are presented, where conditions corresponding to circumstellar envelopes were created: low pressure and a hydrogen-rich environment. The gas concentration in different chambers was set from $\approx 10^8$ to 10^{12} cm^{-3}. The initial gas mixture included hydrogen (H_2) and carbon, and the ratio between the hydrogen and carbon concentrations was $\approx 10^2$, which is lower than the observational estimate of this ratio in stellar envelopes ($\approx 10^3 - 10^4$ [122, 225]) but close to it. The

[7] https://www.nasa.gov/ames/spacescience-and-astrobiology/cosmic-facility.

temperature in the chambers did not exceed 1000 K. According to the experimental results, amorphous carbon particles and aliphatic carbon chains formed in such an environment, while the formation of aromatic molecules and fullerenes was inefficient. At the same facility, Santoro et al. [193] conducted an experiment complementing the preceding one. The initial composition of the gas was changed to include acetylene in addition to hydrogen and carbon. The products contained polyynes, aromatic molecules (benzene, toluene, naphthalene, etc.), hydrogenated and nonhydrogenated carbon clusters, and, finally, nanoscale particles. The last of these were a complex structure consisting of small aromatic islands connected by aliphatic and olefinic bonds. Thus, adding acetylene to the initial gas composition significantly affected the results.

An interesting method for obtaining IDAs was recently proposed in [62]. In that experiment, molecular hydrogen and various carbon particles were mixed, including graphite, fullerenes, and nanotubes. The mixture was then subjected to a process similar to milling. As a result, particles were obtained whose spectra are similar to those of previously obtained IDAs and the spectra of classes $\mathcal{C}$ and $\mathcal{D}$. The authors emphasize that such a process definitely does not occur in the ISM, but this technique can be used for the relatively simple production of IDAs for their further analysis and study, for example, as regards their interaction with UV radiation.

Summarizing the results of the experiments on the synthesis of IDAs, it can be concluded that, under the conditions of AGB star envelopes, particles with a predominantly amorphous structure are formed, which include aromatic islands, both planar and nonplanar, linked to each other by aliphatic or olefinic bonds. Depending on the formation conditions (temperature, pressure, and chemical composition of the initial gas), the particles can differ from each other in the ratio among the numbers of sp, sp^2, and sp^3 bonds, the proportion of hydrogen relative to carbon, size, structure, and other characteristics.

All the above experiments pertain to carbon particles, but SiC particles and probably MgS also form in the envelopes of AGB stars. As noted above, it is assumed that, due to different condensation temperatures, dust grains are not uniform in composition: at solar metallicity, SiC condenses first, and these particles become the cores of dust grains; next, carbon and carbon molecules condense, creating a carbon mantle with an amorphous structure; and finally, the dust grains are covered with a mantle of MgS. At reduced metallicity, SiC particles condense simultaneously with carbon. To the author's knowledge, no experiments simulating the condensation of SiC, carbon, and MgS in stellar envelopes have been conducted, but astrochemical experiments with SiC particles have, as noted above. Merino et al. [125] used prepared silicon carbide particles covered with a graphene layer and bombarded them with hydrogen atoms. The authors believe that this process imitates the possible evolution of dust particles in the outer layers of the envelope, where hydrogen molecules are dissociated by the external UV radiation field. In [125], it was shown experimentally that such bombardment of the surface of silicon carbide results in percolation of the graphene layer and the formation of individual PAH molecules. These PAHs can then desorb into the gas phase under the influence of the UV radiation field.

Another experiment with SiC particles was conducted by Bernal et al. [120]: silicon carbide was heated to ~ 1300 K under a pressure of $\sim 10^{-11}$ atm and irradiated with xenon ions with an energy of 150 keV. This effect was assumed to be similar to the effect of shock waves in a circumstellar envelope. Heating and bombardment led to significant changes in the crystalline structure of the particles. Graphene plates, as well as hemispherical and quasispherical structures with five- and seven-membered rings, were formed in the surface layers. The sizes of nonplanar structures were about 0.7 nm, which is very close to the size of the C_{60} molecule. It follows from this experiment that, under the influence of shock waves or radiation, the structure of SiC particles transforms into a graphene or fullerene-like structure. It can be assumed that, the intensity of the feature at 11.3 μm should decrease with the age of the PPNe and PNe if SiC is present on the dust surface and its structure is destroyed. This correlation has yet to be revealed in observations, while the one between $I_{11.3}$ and the UV radiation hardness, as mentioned above, has already been found.

5.2 Optical properties of interstellar dust analogues

The optical properties of IDAs consisting of amorphous carbon have been deduced both experimentally and theoretically [59, 60, 108, 110, 111, 197, 198, 221, 226–228]. As discussed above, IDAs can differ from each other in the ratio among the number of sp, sp^2, and sp^3 bonds, the fraction of hydrogen relative to carbon, and the size, the shape, and other characteristics, depending on the formation conditions (temperature, pressure, and the chemical composition of the gas during formation). The optical properties of most of the IDA variants proposed in the literature can be used to describe the continuum and the spectral features in the mid-IR range. Overall, the IDA spectra demonstrate good agreement with each other and with observations. However, additional features may arise in the IDA spectra that have not been reliably identified in the spectra of cosmic objects to date. For example, the spectra of the particles studied in [108], along with the features at 21, 27, and 33 μm, which can be identified in PPN and PN spectra, demonstrate a number of features at wavelengths longer than 40 μm which are not observed. Therefore, the search for IDAs with the spectra as close to the PPN and PN spectra as possible continues.

In modern calculations of synthetic spectra of AGB stars, PPNe, and PNe, different versions of the optical properties of carbon particles, in particular, amorphous carbon, are used. For example, in [89], the properties proposed in [230] were used; in [231], those from [110]; and in [113], those from [111]. It is not possible to define a standard for the optical properties, because they all vary with changes in some parameters. In Fig. 11 several versions of the optical properties presented in the literature for IDAs and PAHs in the form of the absorption efficiency factor $Q_{\rm abs}$ are shown. The wavelength range of 3–15 μm, including the main IR bands for particles with a radius of 5 Å (Fig. 11a), and the range of 20–100 μm, reflecting the properties of the continuum for particles with a radius of 100 Å (Fig. 11b), are considered separately.

In a series of studies [2, 59, 197, 198], the optical properties of HAC particles with different hydrogenation degrees (in other words, aromatization or the sp^3/sp^2 ratio) were presented for different particle sizes in a wide range of wavelengths. The sp^3/sp^2 ratio affects both the intensity and position of the IR bands and the color indices. It is evident

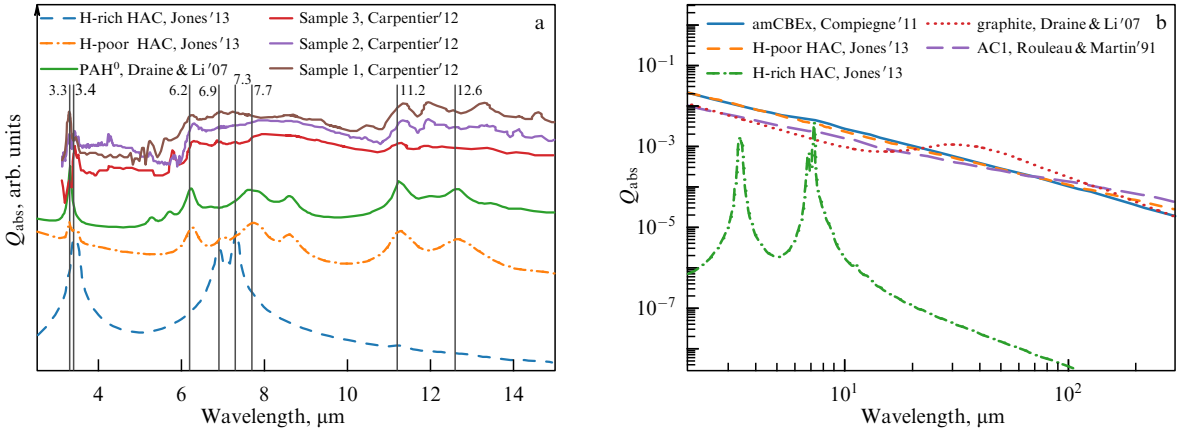

Figure 11. Dependence of absorption efficiency factor of different carbon particles on wavelength. (a) Q_{abs} for hydrogenated (blue line) and dehydrogenated (orange line) HAC particles from [59], PAH from [1] (green line), Sample 3, Sample 2, and Sample 1 particles [61] (red, brown, and purple lines). Efficiency factors are given in arbitrary units and are shifted relative to each other. (b) Q_{abs} for amorphous carbon (amCBEx) from [111, 229] (blue line), hydrogenated (green line), and dehydrogenated (orange line) HAC particles from [59], graphite particles from [1], and amorphous carbon particles from [110]. Particle radii are (a) 5 Å and (b) 100 Å.

from Fig. 11a that the Q_{abs} function for HAC particles with a low H/C ratio (and sp^3/sp^2) is similar to the Q_{abs} function for PAHs: characteristic aromatic bands are present at 3.3, 6.2, 7.7, 11.2, and 12.6 μm. HAC particles with a high H/C ratio (and sp^3/sp^2) have a different Q_{abs} function: the main bands are the aliphatic ones at 3.4, 6.9, and 7.3 μm. The Q_{abs} function for HAC particles from [2] lacks a broad feature near 8 μm observed in $\mathcal{C}$ and $\mathcal{D}$ class objects. The spectrum of Sample 1 particles shows the presence of aromatic bands at 3.3, 6.2, and 8.6 μm and aliphatic bands at 6.9 and 7.3 μm. In the spectrum of Sample 2 particles, the bands at 3.3, 8.6, 6.9, and 7.3 μm become less intense, and the band at 6.2 μm shifts to 6.3 μm, but bands at 3.4 and 8 μm appear. In the spectrum of Sample 3 particles, the band at 3.3 μm disappears, while the band at 3.4 μm becomes intense, the bands at 6.3 and 8.6 μm become even weaker, and the broad feature at 8 μm becomes stronger. The bands at 6.9 and 7.3 μm are present, but they are weaker than in the spectrum of Sample 1 particles. Additional bands appear at ≈ 5.8 and 6.8 μm, possibly having some relation to the nonplanar nature of the material domains. Interestingly, the bands at 11–12 μm are significantly more intense in Sample 1 particles, i.e., in particles with a large number of planar aromatic particles inside, while, in the spectra of Sample 2 and Sample 3 particles, the continuum dominates in this range, and the bands appear weaker.

The material of the Sample 3 particles in [61] contains many curved aromatic molecules, and the sp^3/sp^2 ratio and hence the number of aliphatic bonds are high. It is not possible to unambiguously decide about the characteristics of fullerenes from the presented Sample 3 spectra, because there are no data at wavelengths of 17–20 μm, wherein their specific bands at 17.4 and 18.9 μm fall, and a weaker band at 7.0 μm, which usually appears in fullerene-containing objects, is not visible. Duley et al. [71, 232] studied spectra of amorphous carbon particles obtained by laser ablation of graphite and found bands corresponding to IR transitions in fullerenes, close to those observed in the PN Tc 1 [9], whereas the fullerenes were not recorded in and of themselves as individual molecules. The authors believe that the particles they obtained contain 'protofullerenes,' i.e., nonplanar fullerene-like structures from which fullerenes can be formed when a sample is exposed to external influences (e.g., UV radiation). Thus, amorphous carbon particles with a fullerene-like structure can be responsible for the formation of fullerene bands, while the fullerene molecules themselves are absent. In the experiment in [71], the deposition of amorphous carbon particles formed during graphite ablation was carried out in H_2, He, C_2H_2, and C_2H_4 gases and in a vacuum. The spectra of the deposited particles differ from each other in the intensity and position of the bands. The authors believe that the difference in the position and intensity of the bands in the spectra of laboratory particles and space objects can arise due to the obvious differences among the conditions of formation of amorphous carbon particles.

A similar conclusion about the significant influence of the gas composition was made by the authors of [233], who obtained amorphous carbon particles by laser ablation of graphite in H_2/N_2, H_2/O_2, H_2/CO, and NH_3 gases. The addition of oxygen leads to the suppression of the band at 3.4 μm, a significant decrease in the number of aromatic domains, and an increase in the number of sp^3 bonds. It is important that the band at 3.4 μm is suppressed in the presence of oxygen at a temperature of 300 °C, but appears with the same gas composition at a temperature of 500 °C. Therefore, temperature strongly affects the spectrum of samples, as does the chemical composition of the gas, which must be taken into account when modeling synthetic spectra of dust in space objects. In the spectra of particles obtained in gases containing oxygen and nitrogen, additional bands may appear corresponding to C–N and C–O transitions, which can, in turn, be detected in the IR spectra of space objects.

In Fig. 11b the absorption efficiency factors for larger particles in the long-wavelength part of the spectrum (20–300 μm) are presented. The Q_{abs} function for amCBEx particles is shown, originally calculated in [111] and extrapolated to larger sizes in [229]. The amCBEx particles are HAC particles with a high sp^3/sp^2 ratio, obtained in the laboratory by burning benzene in air under standard conditions. The amCBEx Q_{abs} function is almost featureless, except for a small jump near 8–10 μm. The Q_{abs} function for dehydrogenated HAC in [2] looks similar to the amCBEx function. The Q_{abs} function for AC 1 was calculated in [110] for particles formed in an arc discharge between two amorphous-carbon electrodes [234]. The values of this

function deviate slightly from those of the previous Q_{abs} functions, and the jump in Q_{abs} at $\sim$ 8–10 μm is more noticeable than for amCBEx. The Q_{abs} function for graphite particles calculated in [115] is generally consistent with the functions for the particles already considered, but graphites are characterized by a $\sim$ 30 μm feature, which should manifest itself in the observed spectra. As mentioned above, Otsuka et al. [39] hypothesized that the feature at 30 μm in PPNe and PNe may be associated with graphites, because the intensity of this feature correlates with the continuum, but this hypothesis requires verification. It is possible that graphite particles can be present as part of the HAC particles, similar to how they are present in soot, but additional calculations are required for such particles.

Finally, Fig. 11b shows the Q_{abs} function for the hydrogen-rich HAC in [2]. The values of this function differ significantly (being several orders of magnitude smaller) from the values of all other functions; in addition, there are broad bands at wavelengths of $\sim$ 3 and $\sim$ 8 μm in this case. It was noted in [2] that hydrogenated particles, i.e., 'immature' dust, are characterized by low emissivity, as a result of which the dust, first, is less bright in the long wavelength IR region of the spectrum, and second, is hotter, and therefore the emission peak is shifted to a region of shorter wavelengths. The authors also note that, along with a decrease in emissivity with an increase in sp^3/sp^2, the excess color E(B–V) decreases, i.e., 'immature' dust becomes more transparent in the optical range. At the same time, extinction in the UV range increases. The extinction in the IR range is practically insensitive to sp^3/sp^2. In [2], synthetic spectra of dust are shown for different sp^3/sp^2 ratios. It is noteworthy that 'immature' dust has an emission peak at about 20–30 μm due to the high temperatures of such dust grains. Of course, it is impossible to draw conclusions based on a comparison of these synthetic spectra and the PPN/PN spectra, but the presence of observational features at 21 μm and 30 μm and the theoretical prediction of features at approximately the same wavelengths for 'immature' dust grains arguably means that the coincidence is not accidental. A test would require conducting a detailed modeling of the dust spectra under PPN/PN conditions with the optical properties proposed in [2, 59, 197, 198].

6. Discussion and conclusions

In this section, we summarize the above material and describe possible evolutionary scenarios and processes for carbon particles at different metallicities. In the foregoing, we have discussed (1) observational data on carbon particles in AGB stars, PPNe, and PNe; (2) conditions for dust formation in the envelopes of AGB stars and the evolution of these objects to PNe; (3) mechanisms of the formation of aromatic molecules and large carbon particles; (4) laboratory studies on the formation of IDAs; and (5) optical properties of IDAs. From an observational standpoint, dust evolution proceeds differently, depending on metallicity: at low metallicity, less dust is formed, the relative fraction of PAHs is lower, but the relative fraction of fullerenes is higher. Additionally, there is indirect evidence that the average size of PAHs is smaller at low metallicity and in the presence of fullerenes. The presence of fullerenes in a limited number of objects, together with other observations, indicates that dust formation can branch and follow at least two scenarios, depending on conditions. It is important to find out what factors influence which path evolution will follow. In particular, the answer to the question of why the abundance of PAHs and fullerenes depends on metallicity is of interest. What exactly occurs differently in these objects: formation or destruction?

It has been argued in many papers that dust and PAHs are formed in the same way at low and high metallicities and that the reduced abundance of PAHs at low metallicities is due to destruction. Destruction, namely top-down mechanisms, is also proposed as a source of fullerenes. But the operation of these mechanisms alone cannot explain the fact that fullerenes are distributed nonuniformly over objects with different metallicities, because these mechanisms do not assume a metallicity dependence. At the same time, the process of formation of carbon particles and their final structure depend significantly on many parameters related to metallicity. The combined action of metallicity-dependent dust formation mechanisms and top-down mechanisms can lead to the observed pattern of the PAH and fullerene distribution at different metallicities.

Figure 12 shows a general scheme of the branching of the evolutionary paths of dust particles at different metallicities.

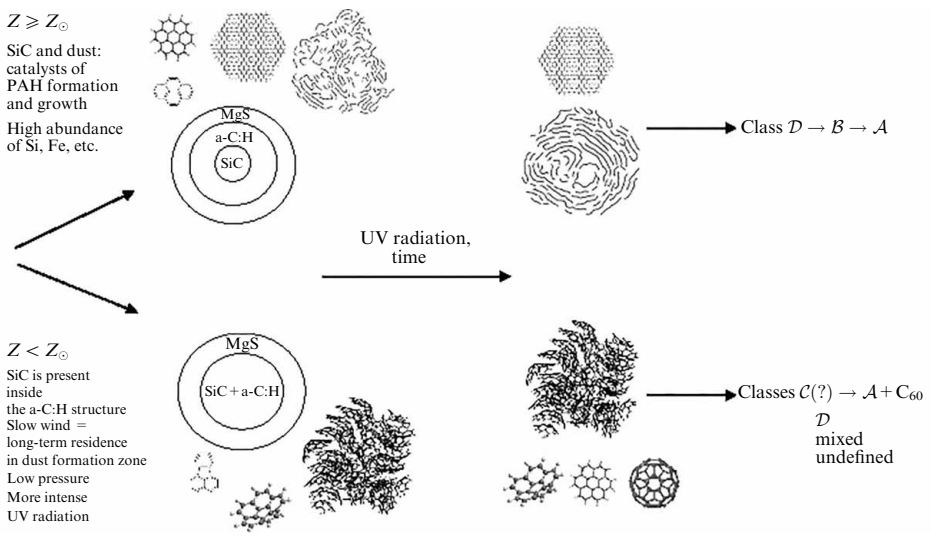

Figure 12. General scheme of the branching of dust evolution scenarios at different metallicities.

Of course, there are no clear boundaries between the media: most likely, both branches of the evolution can occur simultaneously and in the same object, but the probability of evolution along the 'lower' branch (with fullerenes) is higher at a low metallicity, and, accordingly, molecules/particles of this branch should dominate, whereas the probability of the 'upper' branch with larger and planar PAHs is higher at a high metallicity.

The scheme in Fig. 12 is based partly on the results in [61], where it was concluded that differences in the formation conditions lead to differences in the structure of the particle material and the elements of this structure. Under certain conditions, reactions occur that give rise to six-membered rings and hence planar PAHs. In this case, according to [61], the sp^3/sp^2 ratio is the smallest compared to all other particles. Initially, the structure may be irregular, but, under the influence of UV radiation, photodissociation of bonds occurs, the particle structure becomes ordered, and graphite-like inclusions appear in it. Simultaneously with the rearrangement, various fragments in the form of small hydrocarbons and individual PAHs can enter the gas phase from the particle surface. Under other conditions, reactions occur that give rise to five-membered rings and curved PAHs, and a fullerene-like structure of the particle material is formed (Sample 3 particles in [61]). The sp^3/sp^2 ratio and the number of defects in the structure are high. When particles with such a structure are exposed to UV radiation, curved PAHs and fullerenes should presumably be ejected and enter the gas phase. The structure of Sample 2 particles is something between that of Sample 1 and Sample 3: it contains both planar and nonplanar structures. We emphasize that the material of all these particles consists of aromatic molecules linked by aliphatic bonds; the differences are in the size and shape of such molecules and in the number/length of bonds between them.

Based on a comparison of the IR spectra of these particles and of space objects, the authors of [61] conclude that the spectrum of Sample 1 particles corresponds to the transition stage from class $\mathcal{B}$ to class $\mathcal{A}$; the spectrum of Sample 2 particles, to the transition stage from class $\mathcal{C}$ to class $\mathcal{B}$; and the spectrum of Sample 3 particles, to class $\mathcal{C}$. We tend to believe that the spectrum of Sample 1 particles can be attributed to class $\mathcal{D}$ (and D1 at 11–14 μm), which had not yet been introduced at the date of publication of [61]. Subsequently, individual PAHs of a relatively large size can be released from Sample 1 particles; the spectrum of Sample 1 ($\mathcal{D}$) particles thus evolves into the spectrum of class $\mathcal{B}$ and, upon subsequent destruction, into the spectrum of class $\mathcal{A}$. The spectrum of Sample 3 particles, as suggested in [61], is close to the class $\mathcal{C}$ spectra, which are quite rare. The spectrum of Sample 2 particles is a superposition of the spectra of Sample 1 and Sample 3 particles, but these particles are not an evolutionary stage of the transition from Sample 3 to Sample 1 particles. It is possible that objects containing particles similar in structure to Sample 3 and Sample 2 particles (i.e., those containing curved PAHs) can be observed both as class $\mathcal{D}$ objects and as objects that do not fall under the classification, because their structure can be highly inhomogeneous and parts from Sample 1 (with planar PAHs) can be present there.

For Sample 1 through Sample 3, there are no IR spectra at wavelengths of 20–40 μm, and it is therefore impossible to conclude whether features at 21 and 30 μm can appear in their spectra. Grishko et al. [108] could record bands in the spectra of HAC particles near the above wavelengths, and hence they can probably also appear in the Sample 1 through Sample 3 spectra. The unexpected appearance of the feature at 21 μm, as well as the short period of time when it can be observed, indicate that the state of the particle material must be special, unstable, and sensitive to UV radiation. Because the most hydrogenated particles are the most sensitive to UV radiation, it can be assumed that these particles were formed in accordance with the scenario involving planar PAHs with a high H/C ratio. Regarding the feature at 30 μm, in addition to the graphite hypothesis, it is worth testing the hypothesis that this feature is created by particles with a high fraction of hydrogen, which have a lower IR activity than those with a mature structure and are therefore hotter. Their thermal radiation can be superimposed on the radiation of more mature particles from which they are spatially separated.

The authors of [78] put forward a hypothesis that fullerenes are observed at the moment of intersection of the fast and slow winds from a star at the stage of the transition of an AGB star to a PN. According to the authors, during the period of dust condensation, fullerene-like dust and, possibly, some number of fullerenes themselves were formed. The slowly moving dust shell then spreads away from the star, without revealing fullerene radiation, but when the fast wind from the star, which develops later, catches up with this shell, it leads to the destruction of dust (which explains why it is not observed there) and the formation of fullerenes. Otsuka et al. [39] note that all C_{60}-PNe show signatures of powerful winds, and it is therefore possible that wind plays an important role in the formation of fullerenes. In addition to wind, ionizing UV radiation, whose front propagates inside the ejected stellar envelope, can serve as a destructive factor. But whatever the destructive factor, the effective formation of fullerenes during the destruction of dust requires this dust to be 'appropriate,' i.e., fullerene-like.

We summarize the possible factors that can influence the formation of carbon particles.

Silicon carbide abundance. One of the conspicuous observational differences between objects of different metallicities is expressed in the intensity of the SiC band, which is brighter for Galactic objects at the AGB star stage, and for MC objects at the PPN and PN stages. Additionally, the intensity of the SiC band anticorrelates with the intensity of the fullerene bands. Leisenring et al. [90] showed numerically that the condensation temperatures of both SiC and C decrease at low metallicity, which is why SiC and C can condense and settle on the surface simultaneously. It is possible that such a condensation process affects the structure of the carbon material and the size of PAHs. At a low metallicity, the dust grains are covered not by a carbon shell but by a mixed shell of SiC and carbon, and hence, when exposed to UV radiation, the elements of this shell, including small PAHs, curved PAHs, or fullerenes, are desorbed.

The surface of SiC particles can serve as a catalyst for the formation and growth of PAHs [148]. At the solar and higher metallicities, where SiC condenses before the onset of the condensation of carbon particles, SiC particles can serve as a substrate for the accelerated formation and growth of PAHs. At low metallicity values, first, the silicon abundance is lower in absolute quantity, and second, the condensation of SiC occurs with a delay and partially overlaps with the condensation of carbon and carbon particles. Thus, the formation and growth of carbon molecules occurs with a smaller accessible surface area of SiC. As a result, the overall number of PAHs

and amount of dust formed may be lower than at solar metallicity. The importance of heterogeneous reactions occurring both on the SiC surface and on the surface of the hydrocarbon material has not yet been studied in detail, but their importance for the formation of aromatic molecules is discussed in the literature [235], and this issue requires further study.

Wind velocity. If we assume that the wind is slower in low-metallicity stars, then the forming PAH molecules stay longer in the dust formation zone than in the case of high-metallicity stars. The reaction chain leading to the formation of the $C_{40}H_{10}$ molecule (nanobowl) from pentacoranulene includes several cycles of dehydrogenation and cyclization reactions [169], which require energy (see Section 4.1.3). On the one hand, this energy can be available if the molecule is in the dust formation zone. It can be assumed that such a chain of cycles can occur due to the longer stay of the molecules in the high-temperature zone in low-metallicity stars than in high-metallicity stars. On the other hand, dehydrogenation and cyclization of pentacoranulene do not necessarily occur in the dust formation zone. These reactions can occur under the influence of UV radiation already at the PPN or even PN stage, when the central source begins to heat up and generate UV photons. In this case, the presence of a fullerene precursor near the star would also increase the probability of the required chain of dehydrogenation and cyclization, and slower winds in low-metallicity stars can again become a key factor for the formation of fullerenes. In addition, an external radiation field can be the source of UV radiation. It is then important that this radiation penetrate deep enough to reach the formed molecules. In this case, a less dense envelope or an envelope more transparent to UV radiation would contribute to more effective penetration. To satisfy these conditions, a smaller amount of dust must be formed at a lower metallicity, or the dust should have a lower absorption efficiency in the UV range (see below). Both these conditions can be satisfied at low metallicity, and hence the enhanced radiation field in the zone of fullerene precursors can explain their more frequent occurrence at low metallicity. Moreover, the same UV radiation can also initiate a faster dissociation of the formed dust, i.e., top-down mechanisms.

Low absorption efficiency of particles with a fullerene-like structure in UV range. It follows from observations that objects containing fullerenes are bluer in optical color indices [66], while their IR colors do not differ from other objects. Jones et al. [2] presented optical properties for HAC dust grains with different hydrogenation levels. According to that study, HAC particles with a high sp^3/sp^2 ratio and a low aromatization degree give rise to a smaller excess of color in the optical range, E(B–V), than do those with a low sp^3/sp^2 ratio. Sample 3 particles obtained in [61] have a high sp^3/sp^2 ratio and a large number of defects that are characteristic of HAC with a high sp^3/sp^2 ratio in [2]. Although the particles proposed in [2] are not an analogue of particles with a fullerene-like structure, a number of studies [38, 82, 173] put forward a hypothesis that it is precisely such particles that generate fullerenes in PNe. It is likely that a material with a fullerene-like structure can be more transparent in the optical range, just like the most disordered material in [2]. Laboratory measurements and theoretical calculations of the optical properties of materials with a fullerene-like structure are needed to test this hypothesis.

Pressure and* C/O *ratio. Pressure and the abundance of carbon relative to oxygen have a significant effect on the size, shape, and amount of combustion products from an experimental standpoint. The number of fullerenes and small PAHs relative to the volume of soot increases with decreasing pressure, while the absolute amount of soot decreases. Fullerenes are formed in a certain range of C/O values, above or below which they are not formed. Small ($N_C \lesssim 30$) PAHs behave similarly, while large PAHs, on the contrary, grow as the proportion of oxygen increases. Both these experimental results are consistent with observations of fullerenes and PAHs in cosmic objects. First, fullerenes are more likely to be formed at low metallicities, at which the pressure and concentration in the stellar envelopes are lower. Second, the carbon abundance (relative to hydrogen and oxygen) in C_{60}-PNe is lower than in PNe without C_{60}, and the carbon abundance in PNe with the most intense C_{60} bands is lower than in the other C_{60}-PNe. Moreover, for low-metallicity environments, most IR spectra can be assigned to the $\mathcal{A}$ class, i.e., the PAHs in them are on average smaller in size than in high-metallicity environments.

Catalysts. As mentioned above, oxygen influences the formation of carbon molecules and soot. In addition to oxygen, other elements such as iron or nickel can also play an important role. Given that most of the iron is inside the dust [76], catalytic reactions with its participation or with the participation of other heavy elements can possibly occur. The difference in the abundance of heavy elements at different metallicities may lead to a difference in the efficiency of these catalytic reactions. However, to date, catalytic reactions in astrochemistry have been little studied, and the effect of catalysts remains an open question.

To find what factors influence the path of formation of carbon molecules and dust, and to what extent, further experimental and theoretical studies are needed, including modeling of the chemical–dynamical evolution of a star, consistent with the theory of dust formation at different stellar parameters and taking radiation transfer into account. We reiterate that the key parameters may be the oxygen abundance, the abundance of heavy elements and nucleation seeds, including SiC, the rate of the envelope detachment, the corresponding residence time of aromatic molecules and dust seeds in the dust formation zone, the presence of high-velocity winds, etc.

Acknowledgments. The author expresses his gratitude to the referee for a careful reading of the paper, valuable comments, and suggestions; to D S Wiebe (Institute of Astronomy, Russian Academy of Sciences) for research motivation and the useful comments on the data; to Yu A Fadeev (Institute of Astronomy, Russian Academy of Sciences) for discussions and the assistance in study of the evolution of AGB stars; and to E O Pentsak (Zelinsky Institute for Organic Chemistry) for introducing the experimental base for studying carbon materials. The author is very grateful to Romano Corradi for providing the image of the PN NGC 2022 obtained with the New Technology Telescope (NTT, Chile). The archival observational data from the Spitzer Space Observatory (https://sha.ipac.caltech.edu/applications/Spitzer/SHA/) and ISO (https://www.cosmos.esa.int/web/iso/access-the-archive) were used in this study.

The work in Sections 1–3 was carried out in the framework of State Assignment FFWN-2024-0003, and in Sections 4–6, in the framework of State Assignment FEUZ-2020-0038.

References

1. Draine B T, Li A *Astrophys. J.* **657** 810 (2007); astro-ph/0608003
2. Jones A P et al. *Astron. Astrophys.* **558** A62 (2013); arXiv:1411.6293
3. Weingartner J C, Draine B T *Astrophys. J.* **548** 296 (2001); astro-ph/0008146
4. Jones A P et al. *Astron. Astrophys.* **602** A46 (2017); arXiv:1703.00775
5. Hensley B S, Draine B T *Astrophys. J.* **948** 55 (2023); arXiv:2208.12365
6. Allamandola L J, Tielens A G G M, Barker J R *Astrophys. J. Suppl.* **71** 733 (1989)
7. Chiar J E et al. *Astrophys. J.* **507** 281 (1998)
8. Chiar J E et al. *Astrophys. J.* **537** 749 (2000); astro-ph/0002421
9. Cami J et al. *Science* **329** 1180 (2010)
10. Kwok S, Zhang Y *Nature* **479** 80 (2011)
11. Schnaiter M et al. *Astrophys. J.* **498** 486 (1998)
12. Li A, Draine B T *Astrophys. J.* **554** 778 (2001); astro-ph/0011319
13. Steglich M et al. *Astrophys. J. Lett.* **712** L16 (2010); arXiv:1002.3529
14. Mishra A, Li A *Astrophys. J.* **809** 120 (2015); arXiv:1507.06599
15. Campbell E K et al. *Nature* **523** 322 (2015)
16. Campbell E K, Holz M, Maier J P *Astrophys. J. Lett.* **826** L4 (2016)
17. Maier J P, Walker G A H, Bohlender D A *Astrophys. J.* **602** 286 (2004)
18. Salama F et al. *Astrophys. J.* **728** 154 (2011)
19. Omont A, Bettinger H F, Tönshoff C *Astron. Astrophys.* **625** A41 (2019); arXiv:1903.11955
20. Berné O et al. *Astron. Astrophys.* **605** L1 (2017); arXiv:1706.06803
21. McGuire B A et al. *Science* **359** 202 (2018); arXiv:1801.04228
22. McGuire B A et al. *Science* **371** 1265 (2021); arXiv:2103.09984
23. Cherchneff I *Astron. Astrophys.* **545** A12 (2012); arXiv:1111.6809
24. Mattsson L et al. *Mon. Not. R. Astron. Soc.* **440** 1562 (2014); arXiv:1403.0502
25. Matsuura M et al. *Astrophys. J.* **800** 50 (2015); arXiv:1411.7381
26. García-Hernández D A, Górny S K *Astron. Astrophys.* **567** A12 (2014); arXiv:1404.5158
27. Karakas A, Lattanzio J C *Publ. Astron. Soc. Australia* **24** 103 (2007); arXiv:0708.4385
28. Sloan G C et al. *Astrophys. J.* **752** 140 (2012); arXiv:1204.5754
29. García-Hernández D A, in *IAU General Assembly, Meeting 29, August 2015*, id 2254847; arXiv:1511.06165; *Proc. IAU* **11** (A29B) E5 (2015) https://doi.org/10.1017/S1743921317000357
30. Perea-Calderón J V et al. *Astron. Astrophys.* **495** L5 (2009); arXiv:0902.1049
31. Kwitter K B, Henry R B C *Publ. Astron. Soc. Pacific* **134** 022001 (2022); arXiv:2110.13993
32. Chiar J E et al. *Astrophys. J.* **770** 78 (2013)
33. Dartois E *C — J. Carbon Res.* **5** (4) 80 (2019) https://doi.org/10.3390/c5040080
34. Scott A, Duley W W, Pinho G P *Astrophys. J. Lett.* **489** L193 (1997)
35. Draine B T et al. *Astrophys. J.* **663** 866 (2007); astro-ph/0703213
36. Khramtsova M S et al. *Mon. Not. R. Astron. Soc.* **431** 2006 (2013); arXiv:1302.4837
37. Rémy-Ruyer A et al. *Astron. Astrophys.* **563** A31 (2014); arXiv:1312.3442
38. García-Hernández D A et al. *Astrophys. J.* **760** 107 (2012); arXiv:1210.0216
39. Otsuka M et al. *Mon. Not. R. Astron. Soc.* **437** 2577 (2014); arXiv:1310.7711
40. Gordon K D, Clayton G C *Astrophys. J.* **500** 816 (1998); astro-ph/9802003
41. Madden S C et al. *Astron. Astrophys.* **446** 877 (2006); astro-ph/0510086
42. Galliano F, Dwek E, Chanial P *Astrophys. J.* **672** 214 (2008); arXiv:0708.0790
43. Sloan G C et al. *Astrophys. J.* **474** 735 (1997)
44. Hony S et al. *Astron. Astrophys.* **370** 1030 (2001); astro-ph/0103035
45. Peeters E et al. *Astron. Astrophys.* **390** 1089 (2002); astro-ph/0205400
46. Boersma C et al. *Astron. Astrophys.* **511** A32 (2010)
47. Allamandola L J, Hudgins D M, Sandford S A *Astrophys. J. Lett.* **511** L115 (1999)
48. Rosenberg M J F, Berné O, Boersma C *Astron. Astrophys.* **566** L4 (2014); arXiv:1405.5383
49. Andrews H et al. *Astrophys. J.* **807** 99 (2015)
50. Croiset B A et al. *Astron. Astrophys.* **590** A26 (2016); arXiv:1603.02577
51. Boersma C, Bregman J, Allamandola L J *Astrophys. J.* **858** 67 (2018)
52. Maragkoudakis A, Peeters E, Ricca A *Mon. Not. R. Astron. Soc.* **494** 642 (2020); arXiv:2003.02823
53. Sloan G C et al. *Astrophys. J.* **664** 1144 (2007); arXiv:0705.0905
54. Keller L D et al. *Astrophys. J.* **684** 411 (2008); arXiv:0809.2389
55. Acke B et al. *Astrophys. J.* **718** 558 (2010); arXiv:1006.1130
56. Smolders K et al. *Astron. Astrophys.* **514** L1 (2010); arXiv:1004.1967
57. Joblin C et al. *Astron. Astrophys.* **490** 189 (2008); arXiv:0809.1532
58. Mennella V et al. *Astron. Astrophys.* **367** 355 (2001)
59. Jones A P *Astron. Astrophys.* **542** A98 (2012); arXiv:1511.01684
60. Pino T et al. *Astron. Astrophys.* **490** 665 (2008)
61. Carpentier Y et al. *Astron. Astrophys.* **548** A40 (2012)
62. Dartois E et al. *Astron. Astrophys.* **637** A82 (2020); arXiv:2004.02993
63. Shannon M J, Boersma C *Astrophys. J.* **871** 124 (2019); arXiv:1812.02178
64. Matsuura M et al. *Mon. Not. R. Astron. Soc.* **439** 1472 (2014); arXiv:1401.0728
65. Jensen P A et al. *Astron. Astrophys.* **665** A153 (2022)
66. Sloan G C et al. *Astrophys. J.* **791** 28 (2014); arXiv:1406.7034
67. Wagner D R, Kim H, Saykally R J *Astrophys. J.* **545** 854 (2000)
68. Sandford S A, Bernstein M P, Materese C K *Astrophys. J. Suppl.* **205** 8 (2013)
69. Joblin C et al. *Astrophys. J.* **458** 610 (1996)
70. Yang X J et al. *Astrophys. J.* **776** 110 (2013); arXiv:1309.1993
71. Duley W W, Hu A *Astrophys. J.* **761** 115 (2012); arXiv:1210.3222
72. Gadallah K A K, Mutschke H, Jäger C *Astron. Astrophys.* **544** A107 (2012)
73. Papoular R et al. *Astron. Astrophys.* **270** L5 (1993)
74. Ohsawa R et al. *Publ. Korean Astron. Soc.* **32** 87 (2017)
75. Goto M et al. *Astrophys. J.* **589** 419 (2003); astro-ph/0301311
76. Otsuka M *Mon. Not. R. Astron. Soc.* **482** 2354 (2019); arXiv:1810.01703
77. Otsuka M et al. *Mon. Not. R. Astron. Soc.* **462** 12 (2016); arXiv:1607.00936
78. Cami J et al. *Galaxies* **6** 101 (2018)
79. Bregman J D et al. *Astrophys. J.* **344** 791 (1989)
80. Kwok S, Volk K, Bernath P *Astrophys. J. Lett.* **554** L87 (2001)
81. Rapacioli M, Joblin C, Boissel P *Astron. Astrophys.* **429** 193 (2005)
82. Bernard-Salas J et al. *Astrophys. J.* **757** 41 (2012); arXiv:1207.5794
83. Bernard-Salas J et al. *Astrophys. J.* **699** 1541 (2009); arXiv:0905.1124
84. Pitman K M et al., in *Silicon Carbide — Materials, Processing and Applications in Electronic Devices* (Ed. M Mukherjee) (London: IntechOpen, 2011) p. 258, https://doi.org/10.5772/24352
85. Speck A K, Barlow M J, Skinner C J *Mon. Not. R. Astron. Soc.* **288** 431 (1997)
86. Sloan G C et al. *Astrophys. J.* **645** 1118 (2006); astro-ph/0603607
87. Men'shchikov A B et al. *Astron. Astrophys.* **368** 497 (2001)
88. Lagadec E et al. *Mon. Not. R. Astron. Soc.* **376** 1270 (2007); astro-ph/0611071
89. Speck A K et al. *Astrophys. J.* **691** 1202 (2009); arXiv:0810.2599
90. Leisenring J M, Kemper F, Sloan G C *Astrophys. J.* **681** 1557 (2008); arXiv:0803.3067
91. Stanghellini L et al. *Astrophys. J.* **671** 1669 (2007); arXiv:0709.0488
92. Gadallah K A K, Mutschke H, Jäger C *Astron. Astrophys.* **528** A56 (2011)
93. Kwok S *Front. Astron. Space Sci.* **9** 893061 (2022)
94. Ohsawa R et al. *Astrophys. J. Lett.* **760** L34 (2012); arXiv:1211.2385
95. Pino T et al. *Astron. Astrophys.* **490** 665 (2008)
96. Pegourie B *Astron. Astrophys.* **194** 335 (1988)
97. Pitman K M et al. *Astron. Astrophys.* **483** 661 (2008); arXiv:0803.1210
98. Larruquert J I et al. *J. Opt. Soc. Am. A* **28** 2340 (2011) https://doi.org/10.1364/JOSAA.28.002340
99. Volk K, Sloan G C, Kraemer K E *Astrophys. Space Sci.* **365** 88 (2020)

100. Hill H G M, Jones A P, D'Hendecourt L B *Astron. Astrophys.* **336** L41 (1998)
101. von Helden G et al. *Science* **288** 313 (2000)
102. Cox P *Astron. Astrophys.* **236** L29 (1990)
103. Gladkowski M et al. *Astron. Astrophys.* **626** A92 (2019); arXiv:1903.04072
104. Hony S, Waters L B F M, Tielens A G G M *Astron. Astrophys.* **390** 533 (2002); astroph/0204330
105. Nuth J A et al. *Astrophys. J. Lett.* **290** L41 (1985)
106. Zhukovska S, Gail H P *Astron. Astrophys.* **486** 229 (2008); arXiv:0803.2994
107. Jiang B W et al. *Proc. IAU* **9** (S297) 219–222 (2013); arXiv:1307.4014
108. Grishko V I et al. *Astrophys. J. Lett.* **558** L129 (2001)
109. Martin P G, Rogers C *Astrophys. J.* **322** 374 (1987)
110. Rouleau F, Martin P G *Astrophys. J.* **377** 526 (1991)
111. Zubko V G et al. *Mon. Not. R. Astron. Soc.* **282** 1321 (1996)
112. Andersen A C, Höfner S, Gautschy-Loidl R *Astron. Astrophys.* **400** 981 (2003); astro-ph/0210282
113. Srinivasan S et al. *Astron. Astrophys.* **524** A49 (2010); arXiv:1009.2681
114. Ueta T et al. *Astron. Astrophys.* **565** A36 (2014); arXiv:1403.2494
115. Draine B T, Lee H M *Astrophys. J.* **285** 89 (1984)
116. Zijlstra A A et al. *Mon. Not. R. Astron. Soc.* **370** 1961 (2006); astro-ph/0602531
117. Sloan G C et al. *Astrophys. J.* **686** 1056 (2008); arXiv:0807.2998
118. Kwok S, Hrivnak B J, Su K Y L *Astrophys. J. Lett.* **544** L149 (2000)
119. Matsuura M et al. *Mon. Not. R. Astron. Soc.* **382** 1889 (2007); arXiv:0709.3199
120. Bernal J J et al. *Astrophys. J. Lett.* **883** L43 (2019)
121. Sandstrom K M et al. *Astrophys. J.* **744** 20 (2012); arXiv:1109.0999
122. Fonfría J P et al. *Astrophys. J.* **673** 445 (2008); arXiv:0709.4390
123. Lederer M T et al. *Memorie Soc. Astron. Italiana* **77** 1008 (2006)
124. Cherchneff I *Astron. Astrophys.* **526** L11 (2011); arXiv:1012.5076
125. Merino P et al. *Nat. Commun.* **5** 3054 (2014)
126. McCarthy M C, Gottlieb C A, Cernicharo J *J. Mol. Spectrosc.* **356** 7 (2019)
127. Tielens A G G M *Front. Astron. Space Sci.* **9** 908217 (2022); arXiv:2206.01548
128. Höfner S, Olofsson H *Astron. Astrophys. Rev.* **26** 1 (2018)
129. Mattsson L, Wahlin R, Höfner S *Astron. Astrophys.* **509** A14 (2010); arXiv:0909.1513
130. Wachter A et al. *Astron. Astrophys.* **384** 452 (2002)
131. Eriksson K et al. *Astron. Astrophys.* **566** A95 (2014); arXiv:1404.7515
132. Wachter A et al. *Astron. Astrophys.* **486** 497 (2008); arXiv:0805.3656
133. Cummings J D et al. *Astrophys. J.* **818** 84 (2016); arXiv:1601.03053
134. Ventura P et al. *Mon. Not. R. Astron. Soc.* **424** 2345 (2012); arXiv:1205.6216
135. van Loon J T *Astron. Astrophys.* **354** 125 (2000); astro-ph/9912053
136. Corradi R L M et al. *Mon. Not. R. Astron. Soc.* **340** 417 (2003)
137. Mellema G *Mon. Not. R. Astron. Soc.* **277** 173 (1995); astro-ph/9506033
138. Schönberner D *J. Phys. Conf. Ser.* **728** 032001 (2016)
139. Krtička J, Kubát J, Krtićková I *Astron. Astrophys.* **635** A173 (2020) https://doi.org/10.1051/0004-6361/201937150
140. Perinotto M et al. *Astron. Astrophys.* **414** 993 (2004)
141. Schönberner D et al. *Astron. Nachrichten* **335** 378 (2014); arXiv:1404.0391
142. Schönberner D et al. *Astron. Astrophys.* **523** A86 (2010); arXiv:1009.0999
143. Martin J W, Salamanca M, Kraft M *Prog. Energy Combust. Sci.* **88** 100956 (2022) https://doi.org/10.1016/j.pecs.2021.100956
144. Miller J A, Melius C F *Combust. Flame* **91** 21 (1992)
145. Frenklach M, Feigelson E D *Astrophys. J.* **341** 372 (1989)
146. Cole J A et al. *Combust. Flame* **56** 51 (1984)
147. Kaiser R I, Hansen N *J. Phys. Chem. A* **125** 3826 (2021)
148. Zhao T Q et al. *Phys. Chem. Chem. Phys.* **18** 3489 (2016)
149. Gordeev E G, Pentsak E O, Ananikov V P *J. Am. Chem. Soc.* **142** 3784 (2020)
150. Cernicharo J et al. *Astrophys. J. Lett.* **546** L123 (2001)
151. Krestinin A V et al. *Kinet. Catal.* **41** 90 (2000); *Kinetika Kataliz* **41** 102 (2000)
152. Woods P M et al. *Astrophys. J.* **574** L167 (2002)
153. Dong G, Huttinger K *Carbon* **40** 2515 (2002)
154. Kislov V V et al. *J. Chem. Theory Comput.* **1** 908 (2005) https://doi.org/10.1021/ct0500491
155. Parker D S N et al. *Angew. Chem. Int. Ed.* **54** 5421 (2015)
156. Yang T et al. *Angew. Chem. Int. Ed.* **56** 4515 (2017)
157. Zhao L et al. *Nat. Astron.* **2** 413 (2018)
158. Parker D S N et al. *Proc. Natl. Acad. Sci. USA* **109** 53 (2012)
159. Zhao L et al. *Phys. Chem. Chem. Phys.* **22** 22493 (2020)
160. Zhao L et al. *J. Phys. Chem. Lett.* **9** 2620 (2018)
161. Shukla B et al. *J. Phys. Chem. A* **112** 2362 (2008)
162. Xiong S et al. *Comput. Theor. Chem.* **985** 1 (2012)
163. Zhao L et al. *Angew. Chem. Int. Ed.* **58** 17442 (2019)
164. Baum Th et al. *Berichte Bunsenges. phys. Chem.* **96** 841 (1992) https://doi.org/10.1002/bbpc.19920960702
165. Hebgen P et al. *Proc. Combust. Inst.* **28** 1397 (2000)
166. Dunk P W et al. *Nat. Commun.* **3** 855 (2012)
167. Dunk P W et al. *Proc. Natl. Acad. Sci. USA* **110** 18081 (2013)
168. Zhao L et al. *Phys. Chem. Chem. Phys.* **23** 5740 (2021)
169. Tuli L B et al. *Nat. Commun.* **14** 1527 (2023)
170. Homann K-H *Angew. Chem. Int. Ed.* **37** 2434 (1998)
171. Chuvilin A et al. *Nature Chem.* **2** 450 (2010)
172. Zhen J et al. *Astrophys. J. Lett.* **797** L30 (2014); arXiv:1411.7230
173. Micelotta E R et al. *Astrophys. J.* **761** 35 (2012); arXiv:1207.5817
174. Berné O, Tielens A G G M *Proc. Natl. Acad. Sci. USA* **109** 401 (2012); arXiv:1111.0839
175. Murga M S, Akimkin V V, Wiebe D S *Mon. Not. R. Astron. Soc.* **517** 3732 (2022); arXiv:2210.11156
176. Das D et al. *Combust. Flame* **190** 349 (2018)
177. Wang H *Proc. Combust. Inst.* **33** 41 (2011)
178. Jacobson R S et al. *Angew. Chem. Int. Ed.* **59** 4484 (2020)
179. Kholghy M R, Kelesidis G A, Pratsinis S E *Phys. Chem. Chem. Phys.* **20** 10926 (2018)
180. Richter H, Howard J B *Prog. Energy Combust. Sci.* **26** 565 (2000)
181. D'Anna A *Proc. Combust. Inst.* **32** 593 (2009)
182. Frenklach M et al. *Combust. Flame* **188** 284 (2018)
183. Chen T *Astrophys. J.* **866** 113 (2018)
184. Howard J B *Symp. Int. Combust.* **23** 1107 (1991) https://doi.org/10.1016/S0082-0784(06)80371-1
185. Mao Q et al. *J. Phys. Chem. A* **122** 8701 (2018)
186. D'Anna A et al. *Combust. Flame* **127** 1995 (2001)
187. Bowal K, Martin J W, Kraft M *Carbon* **182** 70 (2021)
188. Frenklach M, Mebel A M *Phys. Chem. Chem. Phys.* **22** 5314 (2020)
189. Frenklach M *Phys. Chem. Chem. Phys.* **4** 2028 (2002)
190. Elvati P, Violi A *Proc. Combust. Inst.* **34** 1837 (2013)
191. Menon A et al. *J. Phys. Chem. A* **124** 10040 (2020)
192. Adamson B D et al. *J. Phys. Chem. A* **122** 9338 (2018)
193. Santoro G et al. *Astrophys. J.* **895** 97 (2020); arXiv:2005.02902
194. Mao Q, van Duin A C T, Luo K H *Carbon* **121** 380 (2017)
195. Yuan H et al. *Chem. Eng. Sci.* **195** 748 (2019)
196. Krueger R A, Blanquart G *Combust. Flame* **217** 85 (2020)
197. Jones A P *Astron. Astrophys.* **540** A1 (2012); arXiv:1511.01673
198. Jones A P *Astron. Astrophys.* **540** A2 (2012); arXiv:1511.01682
199. Li W, Shao L *J. Geophys. Res. Atmos.* **114** D09302 (2009) https://doi.org/10.1029/2008JD011285
200. Burlakova V E, Novikova A A *Fullerenes Nanotubes Carbon Nanostruct.* **25** 483 (2017)
201. Leon G et al. *Carbon* **182** 203 (2021)
202. Dhanoa H, Rawlings J M C *Mon. Not. R. Astron. Soc.* **440** 1786 (2014); arXiv:1304.6622
203. Agúndez M, Cernicharo J *Astrophys. J.* **650** 374 (2006); astro-ph/0605645
204. Elvati P, Dillstrom V T, Violi A *Proc. Combust. Inst.* **36** 825 (2017)
205. Peng L et al. *Combust. Flame* **209** 441 (2019)
206. Frenklach M, Ramachandra M, Matula R A *Symp. Int. Combust.* **20** 871 (1985) https://doi.org/10.1016/S0082-0784(85)80576-2
207. Camacho J, Lieb S, Wang H *Proc. Combust. Inst.* **34** 1853 (2013)
208. Salamanca M et al. *Exp. Thermal Fluid Sci.* **43** 71 (2012)
209. Merchan-Merchan W, McCollam S, Pugliese J F C *Fuel* **156** 129 (2015)
210. Serwin M, Karatas A E *Combust. Flame* **229** 111413 (2021)
211. Lebedeva I V et al. *J. Phys. Chem. C* **116** 6572 (2012)
212. Yang X-F et al. *Acc. Chem. Res.* **46** 1740 (2013)
213. Guo J et al. *RSC Adv.* **12** 9373 (2022)

214. de Vries M S et al. *Geochim. Cosmochim. Acta* **57** 933 (1993)
215. Onodera A et al. *J. Appl. Phys.* **69** 2611 (1991)
216. Karatas A, Gülder Ö L *Prog. Energy Combust. Sci.* **38** 818 (2012)
217. Commodo M et al. *Combust. Flame* **219** 13 (2020)
218. Amin H M F, Bennett A, Roberts W L *Proc. Combust. Inst.* **37** 1161 (2019)
219. Gail H P, Sedlmayr E *Astron. Astrophys.* **132** 163 (1984)
220. Martínez L et al. *Nat. Astron.* **4** 97 (2020)
221. Kovačević E et al. *Astrophys. J.* **623** 242 (2005)
222. Jäger C et al. *Astrophys. J.* **696** 706 (2009); arXiv:0903.0775
223. Biennier L et al. *Carbon* **47** 3295 (2009)
224. Contreras C S, Salama F *Astrophys. J. Suppl.* **208** 6 (2013)
225. Cernicharo J *Astrophys. J. Lett.* **608** L41 (2004)
226. Jäger C, Mutschke H, Henning T *Astron. Astrophys.* **332** 291 (1998)
227. Dartois E et al. *Astron. Astrophys.* **423** L33 (2004)
228. Dartois E et al. *Astron. Astrophys.* **432** 895 (2005)
229. Compiègne M et al. *Astron. Astrophys.* **525** A103 (2011); arXiv:1010.2769
230. Hanner M S "Infrared Observations of Comets Halley and Wilson and Properties of the Grains: summary of workshop sponsored by the National Aeronautics and Space Administration, Washington, D.C. and held at Cornell University, Ithaca, New York, August 10–12, 1987," in *NASA Conf. Publication, Summary of a Workshop, Cornell Univ., Ithaca, New York, August 10–12, 1987* (Ed. M S Hanner) (Washington: NASA, 1988)
231. Gómez-Llanos V et al. *Astron. Astrophys.* **617** A85 (2018); arXiv:1806.10248
232. Hu A, Duley W W *Astrophys. J.* **672** L81 (2008)
233. Grishko V I, Duley W W *Astrophys. J.* **568** 448 (2002)
234. Bussoletti E et al. *Astron. Astrophys. Suppl.* **70** 257 (1987)
235. Faccinetto A et al. *Combust. Flame* **158** 227 (2011)